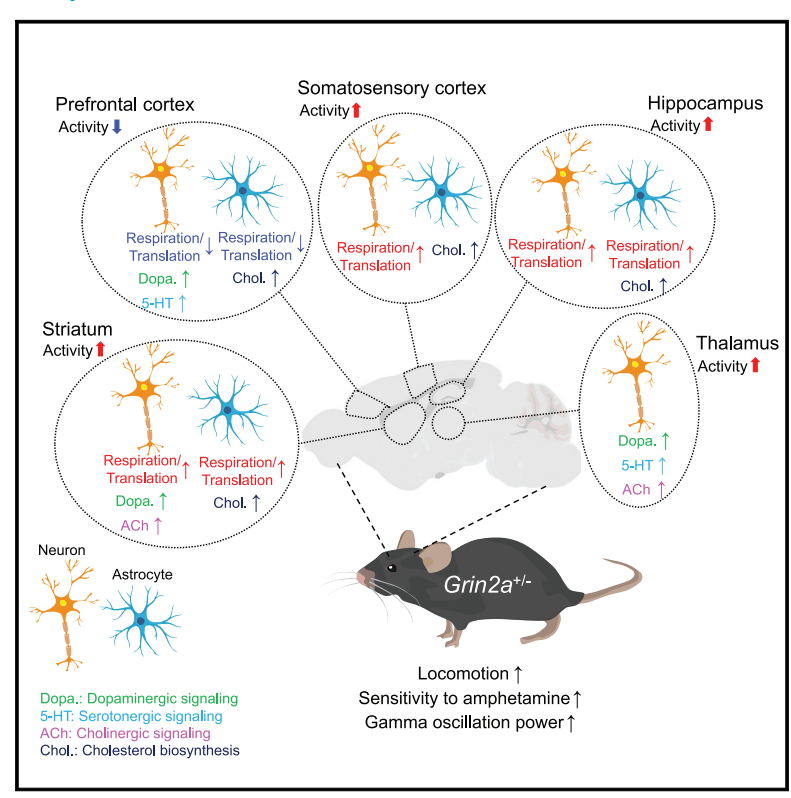
Brain-region-specific changes in neurons and glia and dysregulation of dopamine signaling in *Grin2a* mutant mice

Graphical abstract



Authors

Zohreh Farsi, Ally Nicolella, Sean K. Simmons, ..., Eunjoon Kim, Joshua Z. Levin, Morgan Sheng

Correspondence

zfarsi@broadinstitute.org (Z.F.), msheng@broadinstitute.org (M.S.)

In brief

Farsi et al. show that heterozygous mouse mutants of *Grin2a*, a human schizophrenia risk gene, display major changes at the transcriptomic, proteomic, behavioral, and neurophysiological levels, affecting widespread brain regions, diverse cell types, and multiple signaling pathways, with several abnormal features that resemble schizophrenia patients.

Highlights

- Mice lacking Grin2a, a human risk gene, model several aspects of schizophrenia
- Grin2a^{+/-} mice show prefrontal cortex hypoactivity and hippocampal hyperactivity
- Hyperdopaminergic state in striatum and amphetamine hypersensitivity in Grin2a^{+/-} mice
- Astrocytes, oligodendrocytes, and diverse neuronal types are affected in Grin2a^{+/-} mice



Neuron



NeuroResource

Brain-region-specific changes in neurons and glia and dysregulation of dopamine signaling in *Grin2a* mutant mice

Zohreh Farsi, ^{1,9,*} Ally Nicolella, ¹ Sean K. Simmons, ^{1,2} Sameer Aryal, ¹ Nate Shepard, ¹ Kira Brenner, ¹ Sherry Lin, ³ Linnea Herzog, ¹ Sean P. Moran, ¹ Katherine J. Stalnaker, ¹ Wangyong Shin, ⁴ Vahid Gazestani, ¹ Bryan J. Song, ¹ Kevin Bonanno, ⁵ Hasmik Keshishian, ⁵ Steven A. Carr, ⁵ Jen Q. Pan, ¹ Evan Z. Macosko, ^{1,6} Sandeep Robert Datta, ³ Borislav Dejanovic, ¹ Eunjoon Kim, ^{4,7} Joshua Z. Levin, ^{1,2} and Morgan Sheng ^{1,8,*}

SUMMARY

A genetically valid animal model could transform our understanding of schizophrenia (SCZ) disease mechanisms. Rare heterozygous loss-of-function (LoF) mutations in *GRIN2A*, encoding a subunit of the NMDA receptor, greatly increase the risk of SCZ. By transcriptomic, proteomic, and behavioral analyses, we report that heterozygous *Grin2a* mutant mice show (1) large-scale gene expression changes across multiple brain regions and in neuronal (excitatory and inhibitory) and non-neuronal cells (astrocytes and oligodendrocytes), (2) evidence of hypoactivity in the prefrontal cortex (PFC) and hyperactivity in the hippocampus and striatum, (3) an elevated dopamine signaling in the striatum and hypersensitivity to amphetamine-induced hyperlocomotion (AIH), (4) altered cholesterol biosynthesis in astrocytes, (5) a reduction in glutamatergic receptor signaling proteins in the synapse, and (6) an aberrant locomotor pattern opposite of that induced by antipsychotic drugs. These findings reveal potential pathophysiologic mechanisms, provide support for both the "hypo-glutamate" and "hyperdopamine" hypotheses of SCZ, and underscore the utility of *Grin2a*-deficient mice as a genetic model of SCZ.

INTRODUCTION

Schizophrenia (SCZ) is a disabling mental illness with poorly understood pathophysiology. Existing treatments for SCZ arose from serendipity, have limited efficacy and major side effects, underscoring the need for deeper knowledge of SCZ disease mechanisms. Understanding of SCZ mechanisms has been severely hampered by a lack of animal models that are supported by human genetics.

SCZ has genetic and environmental risk factors, with an estimated heritability of 60%–80%.^{1,2} Many common variants have been identified by genome-wide association study (GWAS) of SCZ, most of which have small effects on disease risk (odds ratio [OR] < 1.1).³ Recent exome sequencing studies have uncovered rare genetic variants associated with SCZ, including protein truncating variants (PTVs)^{4–6} that have large effects on disease risk (OR = 2–60).⁴ The most recent SCZ

exome sequencing meta-analysis (SCHEMA) has identified ten high-confidence genes (hereafter referred to as SCHEMA genes) associated with SCZ at exome-wide significance, including genes encoding synaptic signaling proteins (*TRIO*) and postsynaptic glutamate receptors (*GRIN2A* and *GRIA3*). These SCHEMA variants appear to be predominantly loss-of-function (LoF) mutations, suggesting that heterozygous loss of these genes is sufficient to confer substantial risk of SCZ.^{4,7}

SCHEMA gene LoF mutations can be introduced in mice to create disease models with bona fide human-genetic validity, unlike many previous mouse genetic models of SCZ in which the mutated candidate genes have questionable links to human SCZ. Characterization of SCHEMA mouse mutants by comprehensive approaches can uncover potential disease mechanisms underlying SCZ and also reveal phenotypes at the molecular, cellular, and network levels that can be compared with human data to discover SCZ disease biomarkers.

¹Stanley Center for Psychiatric Research, Broad Institute of MIT and Harvard, Cambridge, MA, USA

²Klarman Cell Observatory, Broad Institute of MIT and Harvard, Cambridge, MA, USA

³Department of Neurobiology, Harvard Medical School, Boston, MA, USA

⁴Center for Synaptic Brain Dysfunctions, Institute for Basic Science, Daejeon, South Korea

⁵Proteomics Platform, Broad Institute of MIT and Harvard, Cambridge, MA, USA

⁶Massachusetts General Hospital, Department of Psychiatry, Boston, MA, USA

⁷Department of Biological Sciences, Korea Advanced Institute for Science and Technology, Daejeon, South Korea

⁸Department of Brain and Cognitive Sciences, Massachusetts Institute of Technology, Cambridge, MA, USA

⁹Lead contact

^{*}Correspondence: zfarsi@broadinstitute.org (Z.F.), msheng@broadinstitute.org (M.S.) https://doi.org/10.1016/j.neuron.2023.08.004



Neuro Resource

GRIN2A, encoding the GluN2A subunit of the NMDA (N-methyl-d-aspartate) receptor (NMDAR), is one of the exomewide-significant SCHEMA genes⁴; additionally, there is strong support for *GRIN2A* as an SCZ risk gene from GWAS fine-mapping.³ Besides SCZ, *GRIN2A* has been associated with neurodevelopmental disorders (NDDs) as well as epilepsy and speech disorders.^{8–11} However, the *GRIN2A* association with SCZ is largely driven by PTVs,⁴ which are almost certainly LoF variants,^{7,12} while associations with NDD and epilepsy are predominantly through missense mutations that are clustered in the transmembrane and linker domains of *GRIN2A*, suggesting an alternate or gain-of-function mechanism.^{11–14}

NMDAR hypofunction has long been hypothesized as a mechanism underlying SCZ pathophysiology, partly because NMDAR antagonists such as phencyclidine or ketamine can induce SCZ-like symptoms in healthy individuals. The discovery of *GRIN2A* as a LoF SCZ risk gene provides indirect human genetics support for the hypo-NMDAR function hypothesis of SCZ. It is notable that *Grin2a* expression peaks postnatally in juvenile rodents, reminiscent of SCZ onset that occurs typically in adolescence and young adulthood. Finally, NMDARs play crucial roles in excitatory synaptic transmission and plasticity, and synaptic dysfunction is implicated in SCZ by human genetics 1,18–20 and by postmortem gene expression studies. 21,22

To gain mechanistic insights into the role of *GRIN2A* in the pathophysiology of SCZ, we performed genome-wide mRNA expression profiling of multiple brain regions in *Grin2a* heterozygous and homozygous knockout mice at several ages as well as proteomic analysis of purified synapses. We studied an existing *Grin2a* knockout mouse line²³ that is representative of multiple SCHEMA PTVs and damaging missense mutations in the *GRIN2A* gene, which are predicted to be null or LoF mutations.^{4,7} For additional insights, we compared the brain transcriptomic profile of *Grin2a* heterozygous mutants with that of *Grin2b* heterozygous knockin mice carrying a null mutation (C456Y) that is associated with autism spectrum disorder (ASD).²⁴ *GRIN2B* encodes the GluN2B subunit of the NMDAR, which is expressed from embryonic stages of brain development, ¹⁶ and has so far not been linked to SCZ.

These comprehensive multi-omics investigations of *Grin2a* mutant mice—combined with our electroencephalogram (EEG) studies showing abnormalities in brain oscillations and automated behavioral analysis (motion sequencing [MoSeq]) showing locomotor perturbations—reveal both unexpected molecular pathway changes (e.g., cholesterol biosynthesis in astrocytes) as well as systems disturbances that support existing theories of SCZ pathobiology (e.g., hyper-dopaminergic state in the striatum). Together, our data builds a molecular-to-systems-level picture of *Grin2a* heterozygous mutant mice as a compelling genetic animal model of SCZ and as a resource for deeper understanding of SCZ disease mechanisms and therapeutics discovery.

RESULTS

Differential effects of *Grin2a* and *Grin2b* LoF on multiple brain regions across development

To capture a comprehensive picture of the brain transcriptome in Grin2a and Grin2b mutant mice across different ages, we first performed bulk RNA sequencing (RNA-seq) analysis on $Grin2a^{+/-}$,

Grin2a^{-/-}, and *Grin2b*^{+/C456Y} mice (*Grin2b*^{C456Y/C456Y} is lethal) and their wild-type (WT) littermates at 2, 4, 12, and 20 weeks of age and across multiple brain regions, including the prefrontal cortex (PFC), hippocampus, somatosensory cortex (SSC), striatum, and thalamus (Figure 1A). The same brain regions from different animals clustered together in the principal-component analysis (PCA), indicating consistency of tissue dissection (Figure S1A).

By bulk RNA-seq, a number of differentially expressed genes (DEGs, see STAR Methods) were identified in both Grin2a and Grin2b mutants in all five brain regions and at all four ages investigated (Figure 1B; Table S1). We validated several DEGs using quantitative real-time PCR, confirming the robustness of the RNA-seq results (Figure S1B). Grin2b+/C456Y showed the most DEGs at 4 weeks (total of 3,591 DEGs across all tested brain regions) as compared with the other tested ages (Figure 1B). In Grin2a mutants, however, the greatest number of DEGs was found at 12 weeks (1,250 in Grin2a+/- and 2,132 in Grin2a-/across tested brain regions) (Figure 1B). Comparing the transcriptomic changes of all individual genes in the same brain region at 12 weeks versus 4 weeks, Grin2a+/- mutants showed larger log₂FC (fold change) at 12 weeks than at 4 weeks in most brain regions (Figures S1C-S1G), whereas Grin2b+/C456Y mutants showed greater changes at 4 weeks of age (Figures S1H-S1L). There were relatively few DEGs for Grin2a or Grin2b mutants at 2 weeks. We therefore concentrated our subsequent analyses on 12 weeks for Grin2a and 4 weeks for Grin2b mutants.

Focusing on differential brain-region effects, we compared the heterozygous mutants $Grin2b^{+/C456Y}$ (4 weeks) versus $Grin2a^{+/-}$ (12 weeks). The hippocampus and striatum showed large transcriptomic changes in both genotypes. The PFC, which is associated with cognitive impairment in SCZ, 25 showed more DEGs in $Grin2a^{+/-}$ than in $Grin2b^{+/C456Y}$ (Figure 1B), whereas the thalamus showed a larger number of DEGs in $Grin2b^{+/C456Y}$. These results suggest that brain regions and circuitries might be differentially affected by Grin2a and Grin2b LoF.

It was notable that Grin2a^{+/-} mice showed comparable numbers of DEGs to Grin2a^{-/-} in most brain regions (see for example, PFC and hippocampus) at all four ages (Figure 1B). A transcriptome-wide comparison showed that log₂FC values of individual genes were moderately well correlated between Grin2a+/- and Grin2a-/- mutants in all brain regions studied (Pearson's r = 0.43-0.77; Figures 1C-1G). These data demonstrate that the transcriptome profiles of the same brain regions are considerably overlapping in Grin2a+/- and Grin2a-/- mutants and that the heterozygous Grin2a LoF has a comparable effect on the overall transcriptome as homozygous Grin2a LoF. By contrast, the transcriptome profile of Grin2a+/- was poorly or even anti-correlated with that of Grin2b+/C456Y in the same brain regions (Pearson's r < 0.1; Figures 1H and 1J-1L), except for the hippocampus (Pearson's r = 0.4; Figure 1I). Thus, loss of one copy of Grin2a or Grin2b causes markedly different global transcriptomic changes at the same age, despite both genes encoding subunits of the NMDARs.

Differential alteration of diverse molecular pathways in brain regions of *Grin2a* and *Grin2b* mutants

To gain insight into the biological processes that were altered in *Grin2a* and *Grin2b* mutant mice, we performed gene set

NeuroResource



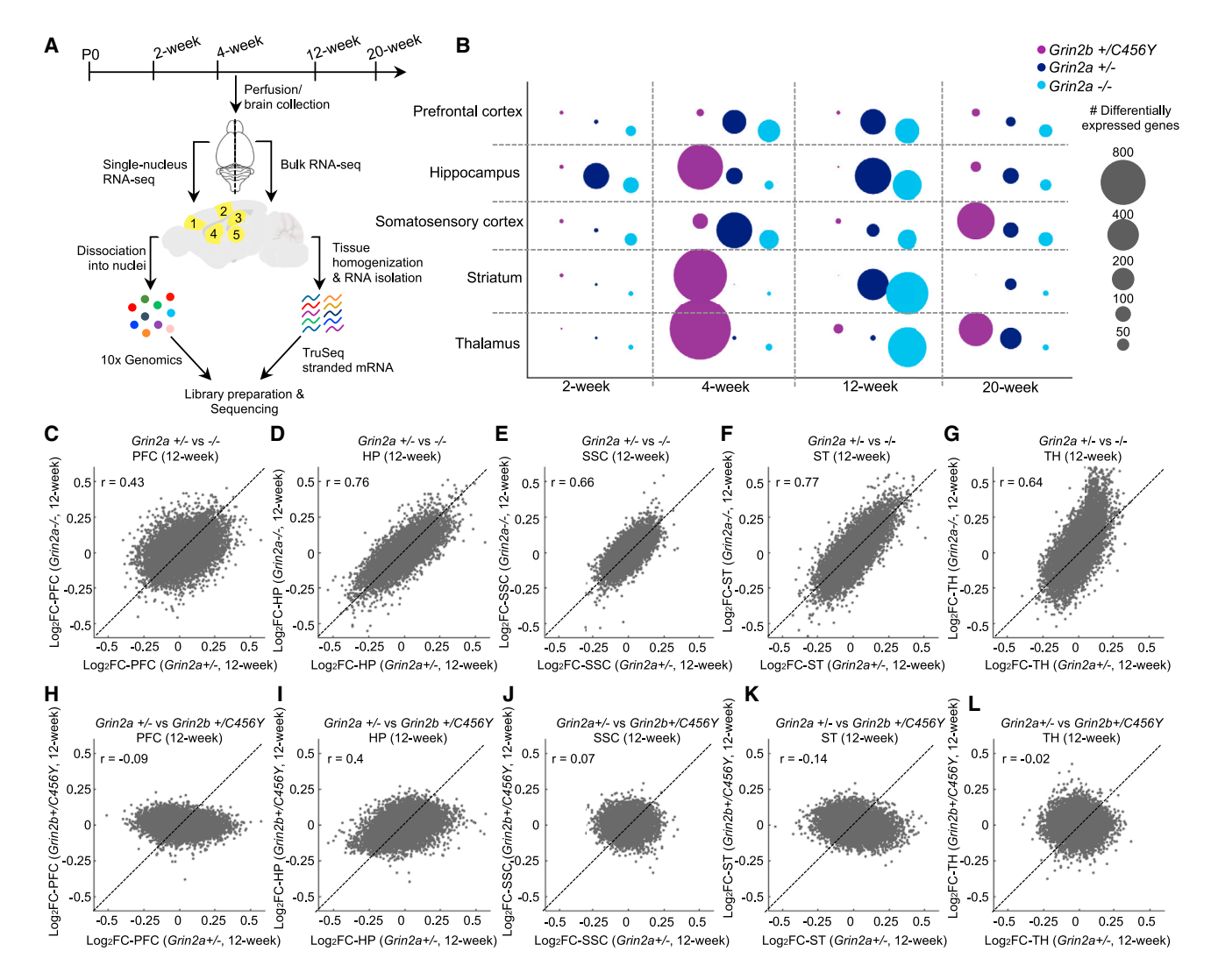


Figure 1. Widespread transcriptomic changes in different brain regions of Grin2a and Grin2b mutant mice (A) Schematic diagram of bulk and snRNA-seq characterization of multiple brain regions in Grin2a and Grin2b mutant mice at four ages. Numbers on the mouse brain indicate (1) prefrontal cortex, (2) somatosensory cortex, (3) hippocampus, (4) striatum, and (5) thalamus. (B) Number of DEGs in the indicated brain region and age in Grin2a and Grin2b mutants. (C-L) Gene expression correlation in the indicated brain regions and genotypes. Pearson's r correlation values are indicated on the plots. See also Figure S1.

enrichment analysis (GSEA)26,27 on bulk RNA-seq data in all brain regions, ages, and genotypes (Table S1). In the GSEA analvsis of 4-week-old Grin2b+/C456Y and 12-week-old Grin2a mutants, a number of pathways (annotated by gene ontology [GO] terms) were found to be significantly (false discovery rate [FDR] < 0.05) enriched among upregulated and downregulated genes (hereafter referred to as upregulated or downregulated pathways/GO terms, respectively) across multiple brain regions. Notably, these "convergent pathways" were related to synapses, ribosomes, oxidative phosphorylation (OXPHOS), neuron development, and RNA processing/splicing (Figure 2A). Similar pathways have been shown to be dysregulated in synaptic proteomics and gene expression studies of postmortem SCZ brain tissue. 21,22,28 In Grin2a+/- and Grin2a-/- mice, neuron development and synaptic GO terms including glutamatergic and gamma-aminobutyric acid (GABA)ergic synapses were downregulated in the PFC and hippocampus, but the same GO terms were upregulated in the striatum (Figure 2A). Consistent with the anti-correlated pathway change, many individual genes within the synapse GO term showed negative correlation in the PFC versus the striatum in Grin2a+/- mice (Pearson's r = -0.23; Figure S1M). This opposite directionality of change in the PFC and hippocampus versus the striatum was also observed in Grin2a mutant mice for OXPHOS and ribosomal GO terms (up in PFC and hippocampus, down in striatum) (Figures 2A, S1N, and S1O). By contrast, in Grin2b+/C456Y mice, OXPHOS and ribosomal GO terms were significantly upregulated in all tested brain regions (Figure 2A).



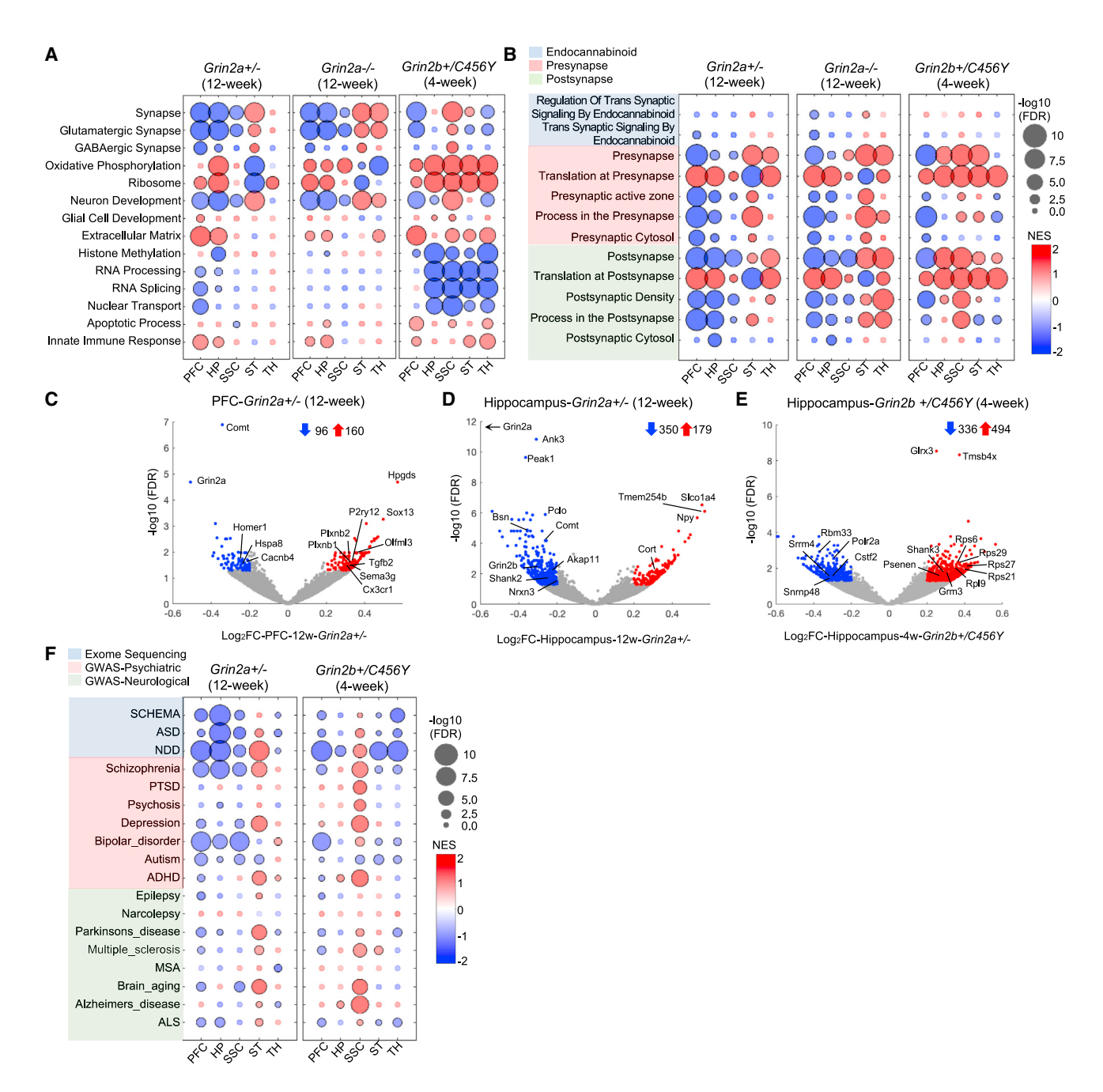


Figure 2. Transcriptomic changes in multiple molecular pathways in Grin2a and Grin2b mutant mice

(A and B) GSEA results for a selection of GO terms from MSigDB (A) and SynGO (B).

(C-E) Volcano plots of transcriptomic changes identified by bulk RNA-seq analysis in the indicated brain regions (blue and red dots represent downregulated and upregulated DEGs, respectively).

(F) GSEA results for risk genes associated with psychiatric and neurological diseases.

In (A), (B), and (F), circles with black outlines indicate statistical significance (FDR < 0.05). In (D), black arrow indicates that Grin2a is out of range of the plot. PTSD, post-traumatic stress disorder; ADHD, attention deficit hyperactivity disorder; MSA, multiple system atrophy; ALS, amyotrophic lateral sclerosis; NES, normalized enrichment score.

See also Figure S1.

Direct comparison of Grin2a+/- at 12 weeks (Figure S1P) and 4 weeks (Figure S1Q) versus Grin2b+/C456Y at 4 weeks confirmed significant enrichment of aforementioned GO terms (such as synapses, OXPHOS, ribosomes) among differentially regulated genes.

GSEA using the refined SynGO terms²⁹ uncovered changes in both presynaptic and postsynaptic processes in Grin2a and Grin2b mutants (Figure 2B). Strikingly, "translation at presynapse" and "translation at postsynapse" GO terms were

NeuroResource



upregulated, whereas GO terms related to pre- and postsynaptic organization were downregulated in the cortex and hippocampus of Grin2a mutants. Downregulation of GO terms related to endocannabinoid signaling, including Dagla (a SCHEMA risk gene with FDR < 0.05⁴), was also observed in the PFC of Grin2a mutants (Figure 2B). Consistent with GSEA analysis, multiple synaptic genes were represented among the downregulated DEGs in the Grin2a+/- mice, such as Homer1 and Cacnb4 in the PFC and Pclo, Bsn, and Shank2 in the hippocampus (Figures 2C and 2D). Like in Grin2a mutants, pre- and postsynaptic translation GO terms were significantly upregulated in the Grin2b+/C456Y cortex and hippocampus (Figure 2B), and many ribosomal genes were among the significantly upregulated DEGs in the hippocampus (Figure 2E; Table S1).

We also tested whether genes associated with psychiatric and neurological disorders (Table S2)30-33 were enriched among differentially regulated genes in Grin2a and Grin2b heterozygous mutants (Figure 2F). In Grin2a+/-, genes associated with multiple brain disorders, notably SCZ (both GWAS and SCHEMA) and ASD were significantly enriched among downregulated genes in the PFC, hippocampus, and SSC and among upregulated genes in the striatum (Figure 2F). Consistent with the association of GRIN2A with NDD,8 NDD-associated genes were also significantly enriched among downregulated genes in the PFC and hippocampus of Grin2a^{+/-} mutants (Figure 2F). In Grin2b mutants, however, genes associated with the same disorders were significantly enriched among upregulated genes in the SSC, further indicating that brain regions are differentially affected by Grin2a and Grin2b LoF. Finally, in line with the overlapping genetic basis of SCZ and bipolar disorder, 34,35 we found a significant enrichment of bipolar GWAS loci among cortical and hippocampal downregulated genes in Grin2a mutants.

Transcriptomic changes in neuronal and non-neuronal cells in Grin2a mutant mice

We performed single-nucleus RNA-seq (snRNA-seq) in Grin2a heterozygous and homozygous mutants and their WT littermates at 12 weeks, when bulk RNA-seq showed the greatest number of DEGs, and at 4 weeks on the PFC and hippocampus. No obvious differences in cell-type clustering were observed between Grin2a mutants and WT mice in any of the tested brain regions (Figures S2A and S2N-S2R). Observed clusters were annotated to different cell types (Figures 3A and S2B-S2E), based on the expression of marker genes (Figures S2F-S2M) and external datasets.

We performed differential expression (DE) analysis using two different algorithms: pseudocell, a mixed model approach that we have recently developed³⁶ (see STAR Methods), and pseudobulk aggregation followed by EdgeR.37 The log₂FC values of individual genes as well as the p values were highly correlated between the two approaches (Pearson's r \geq 0.8 for log_2FC values and Spearman's $r \ge 0.6$ for p values for most cell types) (data not shown). Here, we discuss the results of the pseudocell analysis and provide the DE and GSEA results of pseudobulk analysis for all snRNA-seq datasets in Tables S3 and S4.

In both Grin2a+/- and Grin2a-/-, excitatory neurons such as cortical (PFC, SSC) pyramidal neurons of layer 2/3 (L2/3IT), and layer 5/6 (L5IT and L6CT; Figures 3B and 3C) as well as CA1 pyramidal cells and dentate gyrus excitatory neurons of the hippocampus (Figure 3D) showed large transcriptomic changes at 12 weeks, as measured by the number of DEGs. The inhibitory spiny projection neurons (SPNs) of the striatum (Figure 3E), and DEGLU1 excitatory neurons of thalamus (Figure 3F) also exhibited large numbers of DEGs at 12 weeks. There were fewer DEGs at 4 weeks than at 12 weeks in different cell types in the PFC and hippocampus (Figures 3G and 3H).

Non-neuronal cell types also showed transcriptomic changes by snRNA-seq analysis. Astrocytes and oligodendrocytes (ODCs), in particular, showed a sizable number of DEGs in Grin2a+/- and Grin2a-/- brains, especially in the SSC, hippocampus, and thalamus (Figures 3B-3H). Since glial cells express little or no Grin2a mRNA (Figure S3A), the large transcriptomic changes in astrocytes and ODCs likely reflect the indirect (noncell-autonomous) effects of Grin2a LoF.

It should be noted that a low count of DEGs in certain cell types might be due to low statistical power of detection in those cell types rather than lack of transcriptomic changes. For instance, inhibitory interneurons constituted less than 10% of isolated nuclei from the cortex (PFC and SSC) and less than 5% of hippocampal nuclei (Figures S2N-S2P). The low abundance and high heterogeneity of inhibitory cell types could lead to underestimation of the number of DEGs identified in these cell types by snRNA-seg. In bulk RNA-seg data, we did observe that neuropeptides cortistatin (Cort) and neuropepetide Y (Npv) and/or somatostatin (Sst), which are primarily expressed and released by inhibitory interneurons, 38,39 were among the significantly upregulated DEGs (FDR < 0.05) in the hippocampus of Grin2a^{+/-} (Figure 2D) and Grin2a^{-/-} (Figure S3B) and in the PFC and SSC of Grin2a^{-/-} (Figures S3C and S3D), implying that inhibitory interneurons are affected by Grin2a LoF. Supporting this conclusion, snRNA-seq showed increased expression of a number of neuropeptides including Npy and Cort in the parvalbumin (PV) and somatostatin (SST) interneurons of the PFC, SSC, and hippocampus in *Grin2a*^{+/-} and *Grin2a*^{-/-} (Figures S3E-S3P), though these changes did not reach significance at FDR < 0.05.

Overall, our snRNA-seq data revealed that diverse cell types, including excitatory and inhibitory neurons as well as nonneuronal cells, were affected in Grin2a+/- and Grin2a-/- mutants across the brain regions and at 4 and 12 weeks of age (Figures 3B-3H).

Transcriptomic evidence for altered metabolism and PFC hypofunction in Grin2a mutant mice

Which biological processes are altered in specific cell types in 12-week-old Grin2a mutant mice? Mitochondria/OXPHOSand translation/ribosome-related GO terms showed up commonly as being significantly altered in multiple cell types and brain regions-interestingly not always in the same direction. OXPHOS and ribosomal GO terms were strikingly downregulated in excitatory and inhibitory neurons in the PFC of 12-week-old Grin2a^{+/-} (Figures 4A and S4C) and Grin2a^{-/-} (Figure S4A) mice. In contrast, these GO terms were upregulated in neurons of the hippocampus, striatum, and SSC in Grin2a mutants (Figures 4A and S4A).

Similar region-dependent changes were also observed in 4-week-old $\operatorname{\it Grin2a}^{+/-}$ mice: OXPHOS and ribosomal GO terms



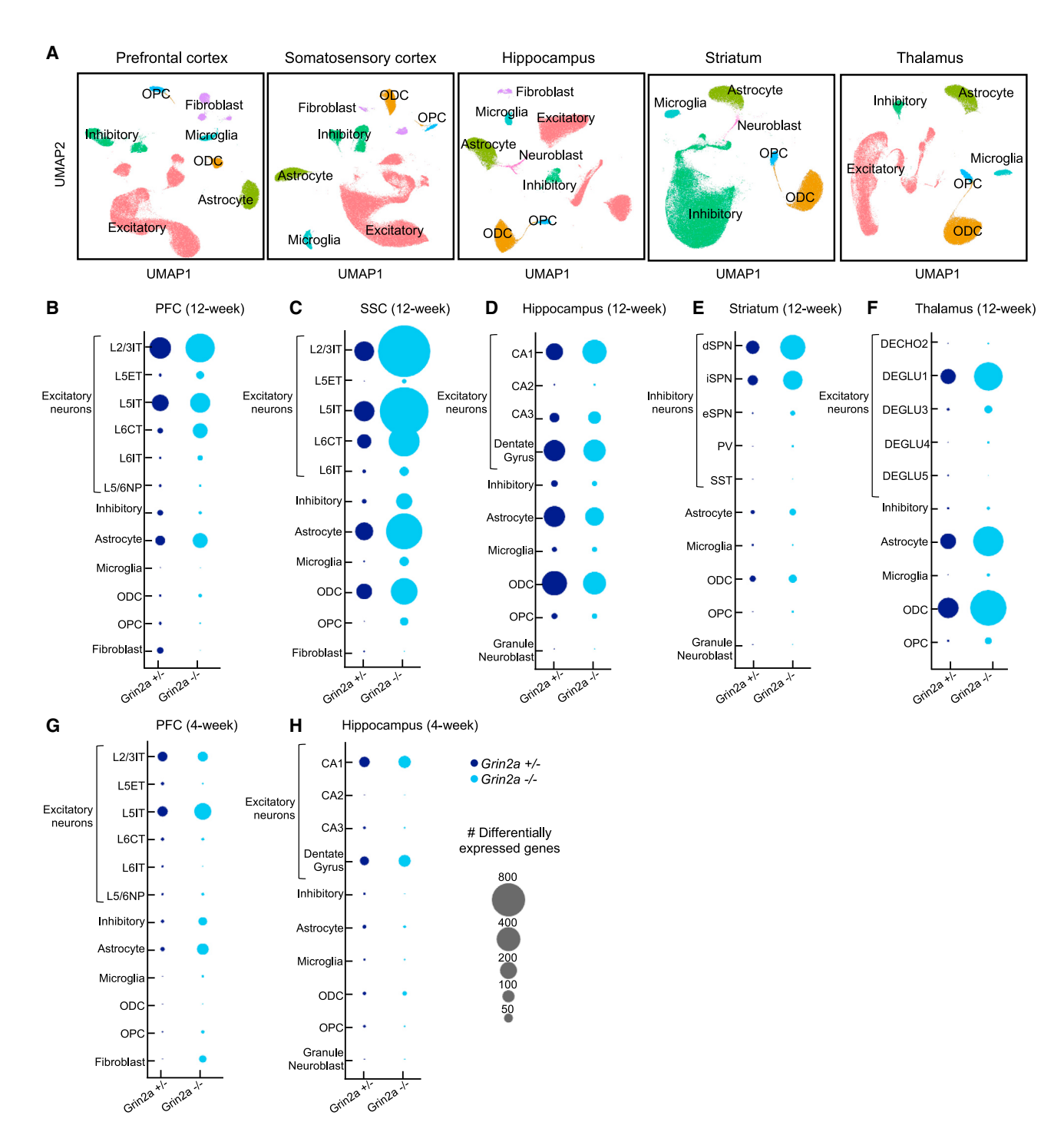


Figure 3. Transcriptomic changes in diverse cell types across brain regions in Grin2a mutant mice

(A) Uniform manifold approximation and projection (UMAP) representation of the major cell types identified by snRNA-seq in the indicated brain regions of Grin2a

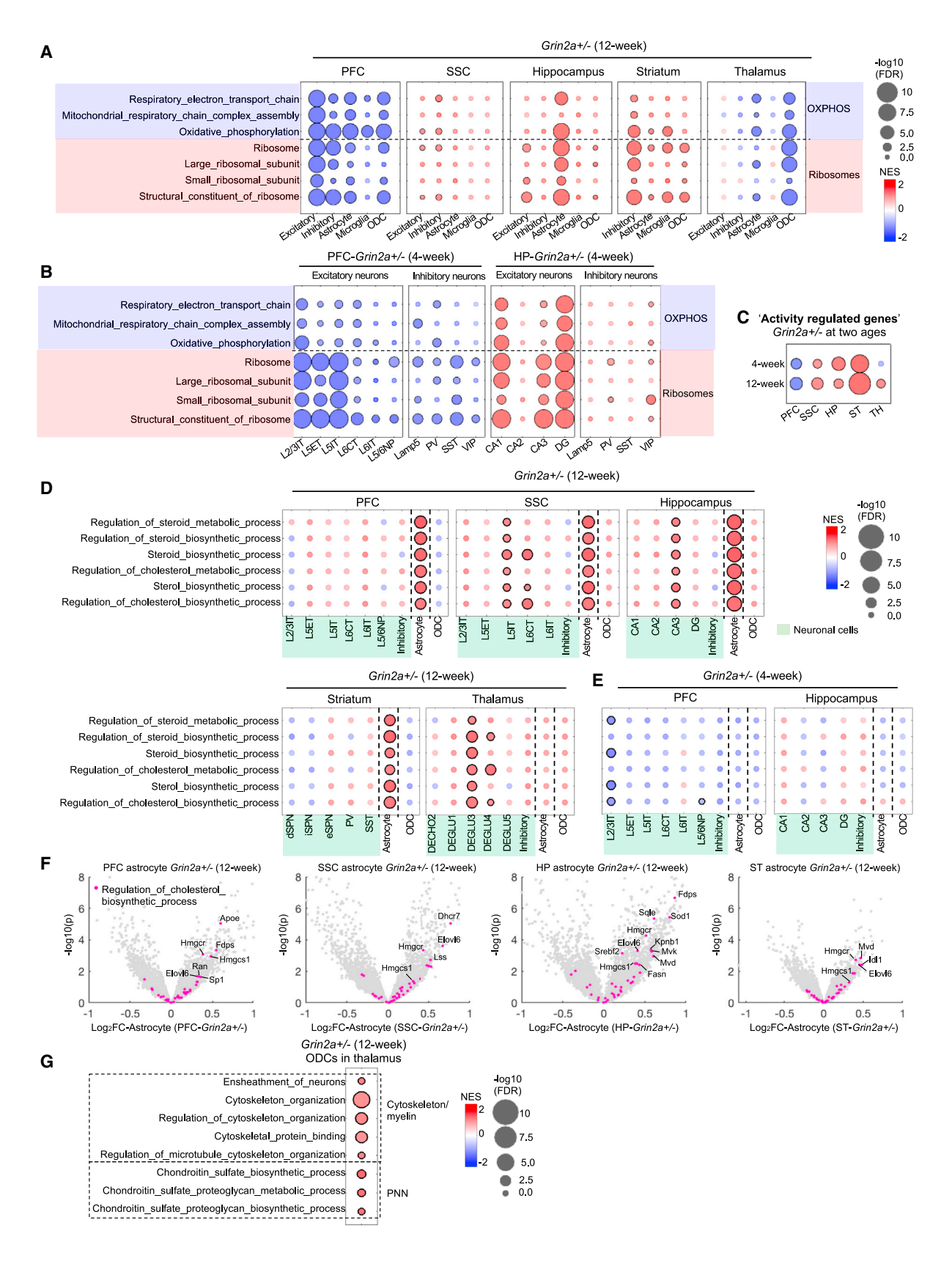
(B-H) Number of DEGs across different cell types in the indicated brain regions.

ODC, oligodendrocyte; PV, parvalbumin interneurons; SST, somatostatin interneurons; VIP, vasoactive intestinal peptide interneurons; L2-L6, layers 2-6; IT, intratelencephalic; NP, near-projecting; ET, extratelencephalic; CT, corticothalamic neuron; dSPN, direct-pathway spiny projection neuron; iSPN, indirectpathway SPN; eSPN, eccentric SPN.

See also Figures S2 and S3.

Neuron NeuroResource





(legend on next page)



Neuron NeuroResource

were significantly downregulated in diverse subtypes of excitatory and inhibitory neurons in the PFC but upregulated in excitatory and inhibitory neuronal subtypes in the hippocampus (Figure 4B). In Grin2a^{-/-} mice at 4 weeks, however, OXPHOS and ribosomal GO terms were upregulated in excitatory and inhibitory neurons of the PFC, which is opposite of what we observed in Grin2a+/- mutants (Figures S4B and S4D). These opposite transcriptomic changes in Grin2a+/- versus Grin2a-/- mutants cannot be simply explained by a gene dosage effect acting via a cell autonomous mechanism.

The changes in OXPHOS and ribosomal GO terms suggest altered adenosine triphosphate (ATP) production and protein translation in Grin2a mutants, which are detectable already at 4 weeks, and that differentially affect the PFC, hippocampus, and striatum. We hypothesized that the altered expression of OXPHOS- and ribosome-related gene sets might reflect the metabolic load or metabolic stress on neurons, which should be influenced by the level of activity in those neurons. As a surrogate measure of neuronal activity, we performed GSEA using a curated set of activity-regulated genes⁴⁰ (Table S2) in various brain regions. Consistent with our hypothesis, the direction of changes in activity-regulated gene set agreed well with changes in OXPHOS and ribosomal GO terms in neurons. PFC showed a significant downregulation of the activity-regulated gene set in Grin2a^{+/-} at 4 and 12 weeks (Figures 4C and S4E), whereas these genes were significantly enriched among upregulated genes in the SSC, hippocampus, and especially the striatum (e.g., Fos, Egr4, and Chrbp; Figure S4F) (Figure 4C). Overall, our RNA-seq data support the idea that the widespread, but regionally distinct, changes in neuronal OXPHOS and ribosomal GO terms may be functionally linked to alterations in neuronal activity. Moreover, they spotlight the PFC as a brain region that potentially has reduced activity and decreased ATP production and protein translation in the heterozygous Grin2a LoF state, in contrast to the SSC, hippocampus, and striatum that show an increase.

Overall, the changes in OXPHOS/ribosome-related GO terms in glial cells were largely correlated with the changes in these GO terms in neurons of the same brain region (Figure 4A). Downregulation of OXPHOS GO terms in microglia, as well as upregulation of "homeostatic" microglial genes P2ry12, Cx3cr1, and Olfml3⁴¹ in the PFC (see Figure 2C), suggest that microglia might be in a more homeostatic state in the PFC of $Grin2a^{+/-}$ mice.

Dysregulation of cholesterol biosynthesis in astrocytes and changes in cytoskeletal organization in ODCs of Grin2a mutant mice

Unexpectedly, GO terms related to cholesterol/steroid biosynthesis (including genes Hmgcr, Hmgcs1, Elovl6, Srebf2) were significantly upregulated in astrocytes of the PFC, SSC, hippocampus, and striatum in $Grin2a^{+/-}$ (Figures 4D and 4F) and Grin2a^{-/-} mutants (Figures S4H and S4J). The upregulation of cholesterol-related GO terms was also significant in some subtypes of excitatory neurons in the SSC, hippocampus, and PFC (Figures 4D and S4H). In the thalamus, the cholesterol pathway changes were most prominent in DEGLU3 excitatory neurons (Figures 4D and S4H).

Dysregulation of the cholesterol biosynthesis pathway in astrocytes was significant at 12 weeks but not at 4 weeks (Figures 4E and S4I), and most cholesterol-related genes showed larger changes at 12 weeks than at 4 weeks (Figure S4K). Thus, the alteration in cholesterol biosynthesis pathway occurs relatively late during postnatal brain maturation in Grin2a mutant mice.

In ODCs of the thalamus, besides OXPHOS and ribosomal GO terms, pathways related to the cytoskeleton and neuron ensheathment (including myelination-related genes such as Gal3st1, Ilk, Klk6⁴²) were significantly upregulated, suggesting potential myelin abnormalities in the thalamus of Grin2a+/mice (Figure 4G). Moreover, GO terms related to biosynthesis of chondroitin sulfate (which is enriched in the perineural net [PNN]) were significantly upregulated in thalamic ODCs in $Grin2a^{+/-}$ mice (Figure 4G).

Dysregulation of dopamine signaling in the striatum of Grin2a mutant mice

Of particular interest, various GO terms related to dopaminergic and cholinergic signaling were significantly upregulated in the inhibitory neurons of the striatum (~95% of which are SPNs; Figure S2D) in 12-week-old Grin2a+/- mice (Figure 5A) but not in Grin2a^{-/-} mice (Figure S5A).

Multiple genes within the "response-to-dopamine" and "synaptic-transmission-cholinergic" GO terms (e.g., Chrm3, Slc5a7, Chrm2, Drd2, and Lrrk2) were elevated in the striatal inhibitory neurons of 12-week Grin2a+/- mice (Figures 5B and 5C). It did not escape our attention that Drd2 (D2 dopamine receptor, the target of most antipsychotic drugs) was among the most highly upregulated genes in the striatal inhibitory neurons (Figure 5B).

Activation of transcription factor cyclic adenosine 3',5'-monophosphate (cAMP) response element-binding protein (CREB) via mitogen-activated protein kinase (MAPK) pathways plays a vital role in dopamine receptor signaling.⁴³ GO terms related to positive regulation of CREB activity and MAPK pathways were significantly upregulated in the striatal neurons of Grin2a^{+/-} mice (Figure 5A), along with elevated expression of several cAMP-induced CREB target genes in direct-pathway SPNs (dSPNs) and indirect-pathway SPNs (iSPNs)⁴⁴ (Figure S5B; Table S2). Extending these results, we found a significant enrichment of a set of dopamine-induced genes (Table S2; including

Figure 4. Brain-region-specific effects on activity-, metabolism-, and cholesterol-related pathways in neuronal and non-neuronal cells in Grin2a+/- mice

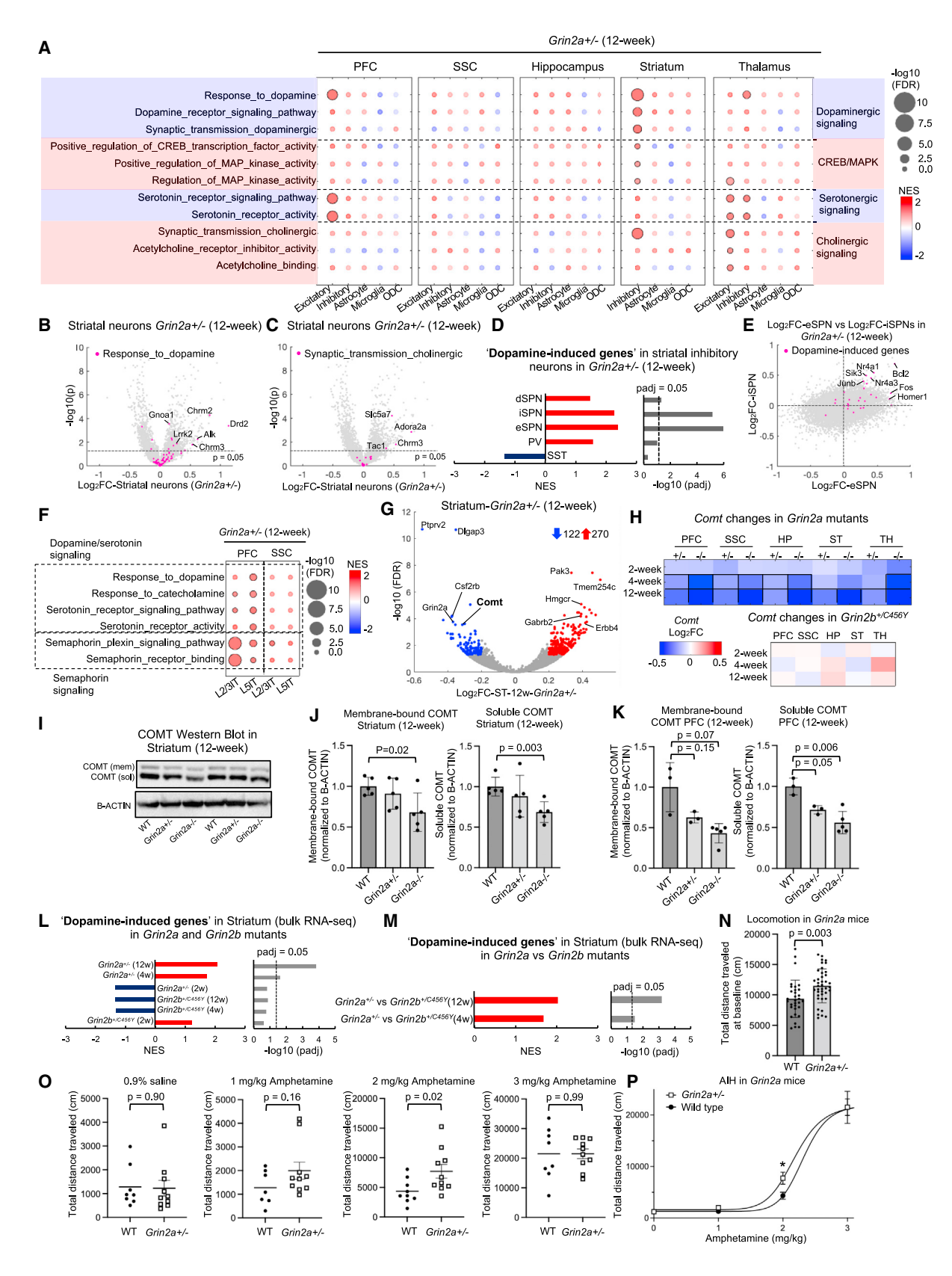
(A and B) GSEA results for five major cell types (A) and across neuronal subtypes (B) in the indicated brain regions of Grin2a^{+/-}.

- (C) Enrichment of the activity-regulated gene set in different brain regions (bulk RNA-seq) of Grin2a+/-.
- (D and E) GSEA results for the indicated GO terms in the indicated brain regions of Grin2a+/-
- (F) Volcano plots of transcriptomic changes in astrocytes in the indicated brain regions of Grin2a+/- highlighting genes from the indicated GO term.
- (G) GSEA results for the indicated GO terms in thalamic oligodendrocytes of Grin2a+/-.

See also Figure S4.

NeuroResource





(legend on next page)



Neuron NeuroResource

activity-regulated genes Homer1, Fos, and Junb that are induced by dopamine⁴⁵) among the upregulated genes of the Grin2a^{+/-} striatum (Figure 5D). Notably, the upregulation of the dopamine-induced gene set was particularly strong in iSPNs which express mainly D2 dopamine receptors, and in eccentric SPNs (eSPNs) which express both D2 and D1 receptors (Figures 5D and 5E).

We also found evidence for altered dopamine and serotonin signaling in the PFC of 12-week-old Grin2a+/- mice, where dopamine and/or serotonin signaling GO terms were significantly upregulated in L2/3IT and L5IT pyramidal cells (Figure 5F). These same cell types also showed significant upregulation of GO terms related to semaphorin-plexin signaling (Figure 5F), which is known to be involved in the remodeling of synaptic connections⁴⁶⁻⁴⁸ and has been implicated in SCZ.^{49,50} Plexins Plxnb1 and Plxnb2 and semaphorin Sema3g were among the significantly upregulated DEGs in the PFC of 12-week-old Grin2a+/- mice (Figure 2C). Most of these GO terms related to dopamine, serotonin, or semaphorin signaling did not change significantly in the SSC of Grin2a+/- (Figure 5F) mice, or in the PFC and SSC of $Grin2a^{-/-}$ mice (Figure S5C).

In the context of heightened dopamine signaling, it is noteworthy that Comt (encoding catechol-O-methyltransferase, an enzyme involved in dopamine degradation) was among the most significantly downregulated genes in the bulk RNA-seg analysis of striatum in 12-week-old Grin2a^{+/-} mice (Figure 5G). In fact, Comt mRNA was consistently reduced in a gene-dose-dependent fashion in all tested brain regions of Grin2a mutants (Figure 5H). In contrast, Grin2b+/C456Y mutants showed no significant changes in Comt mRNA in any brain region (Figure 5H). We confirmed reduction of COMT protein by western blotting: COMT levels fell by ${\sim}50\%$ in the PFC and ${\sim}40\%$ in the striatum in 12-week-old Grin2a^{-/-} mice, with Grin2a^{+/-} mice showing intermediate reduction (Figures 5I-5K). Decreased expression of Comt might lead to elevated dopamine levels and contribute to the enhanced expression of dopamine-induced genes in the striatum of Grin2a^{+/-} mice

(Figure 5D). Consistent with such a notion, we observed a significant enrichment of the dopamine-induced gene set among upregulated genes of the striatum in Grin2a+/- mutants at 4 and 12 weeks, but not at 2 weeks, suggesting that striatal dopamine dysregulation emerges during the juvenile period in Grin2a+/mice (Figure 5L). In the striatum of Grin2b+/C456Y mutants, however, there was no significant change of the dopamine-induced gene set at any of the tested ages (Figure 5L). Direct comparison of Grin2a+/- versus Grin2b+/C456Y mutants also showed significant upregulation of dopamine-induced gene set in the Grin2a^{+/-} striatum (Figure 5M). Together, the transcriptomics data point to dysregulated dopamine signaling, suggestive of a hyperdopaminergic state in the striatum and PFC of specifically Grin2a+/- mice. To test this idea functionally, we measured amphetamine-induced hyperlocomotion (AIH) in $Grin2a^{+/-}$ mice across various doses of amphetamine (Figure S5D). Compared with their WT littermates, Grin2a+/- mice showed significantly greater baseline locomotor activity (Figure 5N) and enhanced responses to submaximal doses of amphetamine (1 and 2 mg/kg), reaching significance at 2 mg/kg of amphetamine (Figure 50). The leftward shift of the dose-response curve demonstrates the greater sensitivity of Grin2a^{+/-} mutants to AIH (Figure 5P), supporting our hypothesis of elevated dopamine sensitivity in the striatum of *Grin2a*^{+/-} mice.

In the thalamus, serotonin and cholinergic signaling GO terms were significantly upregulated in the excitatory neurons of Grin2a^{+/-} mice (Figure 5A). A significant upregulation of some dopaminergic/serotoninergic signaling pathways was also observed in the inhibitory neurons of the thalamus in both Grin2a^{+/-} (Figure 5A) and Grin2a^{-/-} (Figure S5A) mice, including genes Htr2a and Htr2c (serotonin receptors 2A and 2C) (Figure S5E).

Changes in glutamatergic signaling and ribosomal proteins in the synaptic proteome of Grin2a mutant mice

To investigate the effects of Grin2a LoF on synapses at the protein level, we conducted quantitative mass spectrometry (MS)

Figure 5. Dysregulation of dopamine signaling in the striatum of *Grin2a*+/- mutant mice

- (A) GSEA results for five major cell types in the indicated brain regions of Grin2a+/-
- (B and C) Volcano plots of transcriptomic changes in striatal inhibitory neurons in Grin2a^{+/-} highlighting genes from the indicated GO terms.
- (D) Enrichment of the dopamine-induced gene set in striatal inhibitory neuron subtypes in Grin2a+/-.
- (E) Transcriptomic changes in eSPNs versus iSPNs in the striatum of Grin2a+/-, highlighting the dopamine-induced gene set.
- (F) Changes in the indicated GO terms in layer 2/3IT and layer 5IT excitatory neurons in the PFC and SSC of Grin2a+1
- (G) Volcano plot of transcriptomic changes identified by bulk RNA-seq analysis in the striatum of 12-week-old Grin2a+/- mice. Genes of interest are labeled on the volcano plot.
- (H) Heatmap showing the log₂FC values of Comt in the bulk RNA-seq data from the indicated brain regions in Grin2a and Grin2b mutant mice. Black outlines indicate statistical significance (FDR < 0.05).
- (I) Western blots probing for COMT and B-actin in total striatal lysate obtained from 12-week-old Grin2a animals.
- (J and K) Quantification of COMT protein expression measured by western blot in the striatum (J) and PFC (K) of Grin2a animals (n = 3-5 animals per genotype). (L and M) Enrichment of the dopamine-induced gene set in the striatum (bulk RNA-seq) in $Grin2a^{+/-}$ and $Grin2b^{+/C456Y}$ (L) mice and in $Grin2a^{+/-}$ versus Grin2b+/C456Y comparison (M) animals.
- (N) Basal locomotion in wild-type and Grin2a+/- mice before administration of saline/amphetamine (n = 32 wild type; n = 40 Grin2a+/-).
- (O) Total distance traveled after administration of saline or amphetamine in wild type or Grin2a+/- (n = 7-9 wild types per amphetamine dose; n = 10 Grin2a+/- per amphetamine dose).
- (P) Dose-response curves for wild-type and $Grin2a^{+/-}$ mice. The lines indicate a nonlinear regression four-parameter fit to each dataset. The asterisk indicates the dose at which Grin2a+/- is significantly different from wild types.
- In (J), (K), and (N)-(P), p values are computed using two-tailed Student's t test. Data are shown as mean ± standard error in (J), (K), (N), and (O) and as mean ± standard error of mean in (P). CREB, cyclic adenosine 3',5'-monophosphate (cAMP) response element-binding protein; MAPK, mitogen-activated protein kinase; WT, wild type.

See also Figure S5.

NeuroResource



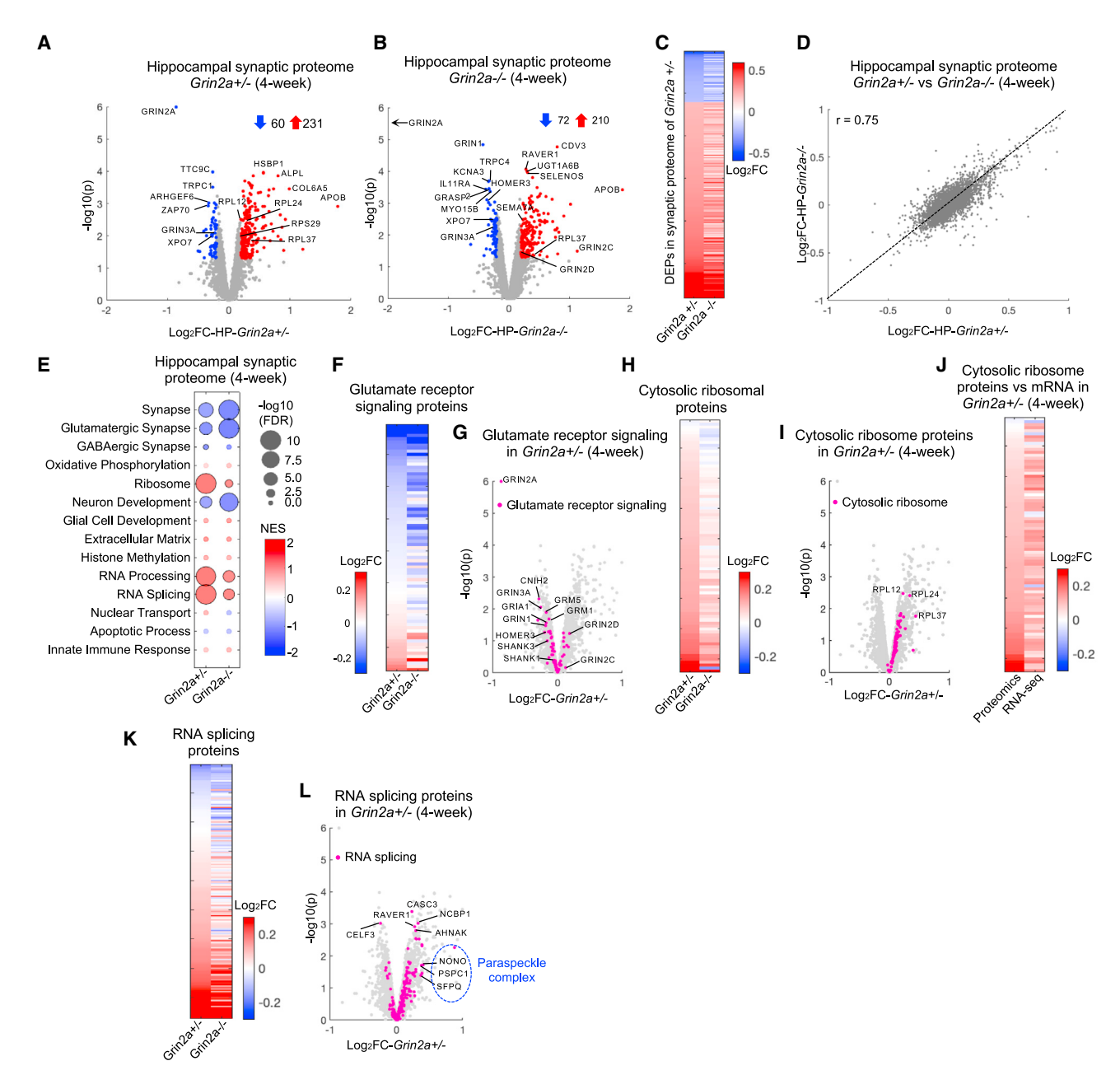


Figure 6. Synapse proteome changes in Grin2a mutant mice

- (A and B) Volcano plots of proteomic changes in the hippocampal synapses of 4-week-old $Grin2a^{+/-}$ (A) and $Grin2a^{-/-}$ (B) mice.
- (C) Heatmap showing log_2FC values in $Grin2a^{+/-}$ and $Grin2a^{-/-}$ for significant DEPs identified in the hippocampal synapses of $Grin2a^{+/-}$.
- (D) Correlation of protein changes in the hippocampal synapses of $Grin2a^{+/-}$ versus $Grin2a^{-/-}$ (Pearson's r = 0.75).
- (E) GSEA results in the hippocampal synapse proteome of 4-week-old *Grin2a*^{+/-} and *Grin2a*^{-/-}.
- (F, H, and K) Heatmap depicting proteins in the indicated gene set in the synaptic proteome of 4-week-old *Grin2a*^{+/-} and *Grin2a*^{-/-} mice.
- (G, I, and L) Volcano plots of proteomic changes in Grin2a+/- synapses highlighting proteins in the indicated gene sets.
- (J) Heatmap depicting proteins in the indicated gene set in the synaptic proteome and their mRNA changes in bulk RNA-seq data in the hippocampus of 4-week-old *Grin2a*^{+/} mice.

In (C), (F), (H), (J), and (K), rows are sorted in ascending order based on the log_2FC values from $Grin2a^{+/}$. See also Figure S6.

proteomics of synaptic fractions purified from the hippocampus of 4-week-old $Grin2a^{+/-}$ and $Grin2a^{-/-}$ mice and their WT littermates. The synapse fractions showed strong enrichment of ca-

nonical synaptic markers (GluN1, PSD95, HOMER1) (Figure S6A). We observed a similar number of differentially expressed proteins (DEPs, see STAR Methods) in *Grin2a*^{+/-}



Neuron NeuroResource

(Figure 6A; 291 DEPs) and $Grin2a^{-/-}$ mice (Figure 6B; 282 DEPs), and validated several of them by western blotting (Figures S6B and S6C). The vast majority (97%) of the DEPs in Grin2a+/mice were also altered in the same direction in Grin2a^{-/-} (Figure 6C), such as GRIN3A, RPL37, and XPO7 (Figures 6A and 6B). Evaluation of the log₂FC values of all individual proteins revealed a strong correlation and a similar magnitude of change of the synaptic proteomes in Grin2a+/- and Grin2a-/- mice (Pearson's r = 0.75; Figure 6D). Overall, these data signify that heterozygous Grin2a LoF has a similar-size effect on global synapse composition as homozygous LoF, which is in line with our conclusion from bulk RNA-seq data that Grin2a+/- has comparable effect as $Grin2a^{-/-}$ on the transcriptome (Figure 1B)

GSEA of the proteomics data showed that GO terms related to synapses, particularly glutamatergic synapses, were significantly downregulated in synapses of Grin2a mutants (Figure 6E). There was a positive though weak correlation between synaptic proteomic changes and bulk RNA-seq changes in the glutamatergic signaling pathway in the 4-week-old hippocampus (Figures S6D and S6E). Perhaps not surprising because GRIN2A is itself a glutamate receptor, the magnitude of reduction of many downregulated proteins of glutamatergic signaling was greater in Grin2a^{-/-} than in Grin2a^{+/-} (Figure 6F). Many glutamate receptor subunits (e.g., GRIN1, GRIN3A, GRM5, GRIA1, and GRIA2) and the scaffolding proteins SHANK1, SHANK3, and HOMER3 were among the downregulated proteins in both $Grin2a^{+/-}$ (Figure 6G) and $Grin2a^{-/-}$ (Figure S6F).

GO terms related to ribosomes and RNA processing/splicing were significantly upregulated in Grin2a mutant synapses (interestingly, to a greater degree in $Grin2a^{+/-}$ than in $Grin2a^{-/-}$) (Figures 6E, 6H, and 6K), Ribosomal proteins showed striking elevation as a group in the synapses of Grin2a+/- mice (Figure 6I) and, to a lesser extent, in Grin2a^{-/-} mutant mice (Figure S6G), potentially pointing to increased protein synthesis at synapses of Grin2a mutants. The increase in ribosomal proteins is consistent with the elevated ribosomal gene expression in bulk RNAseq data from the 4-week-old hippocampus (Figures S6H and S6I) and in snRNA-seq data from excitatory neurons and inhibitory interneurons in the hippocampus of 4-week-old Grin2a mutants (Figures 4B and S4B). More than 90% of ribosomal proteins that were upregulated in the synaptic proteome of Grin2a+/- and Grin2a-/- were also upregulated at the mRNA level in bulk RNA-seq analysis of the hippocampus in 4-weekold Grin2a mutant brains (Figures 6J and S6J). However, the correlation of the log₂FC values of mRNA and synaptic protein level of the ribosomal genes was only modest (r = 0.3-0.4) (Figures S6K and S6L), suggesting that post-transcriptional changes, such as protein turnover and trafficking, likely contribute to ribosomal protein changes at synapses in Grin2a

Surprisingly, more than 60% of identified RNA splicing proteins were elevated in Grin2a+/- (Figures 6K and 6L) and Grin2a^{-/-} synapses (Figure S6M), including proteins of the paraspeckle complex (SFPQ, NONO, and PSPC1). Paraspeckles are subnuclear bodies involved in transcription initiation, transcriptional termination, and mRNA splicing.51 The presence and increased abundance of the paraspeckle complex and other RNA processing/splicing proteins in synaptic fractions of Grin2a

mutants might indicate mislocalization of these RNA binding proteins from the nucleus to the cytoplasm, a pathomechanism that has been implicated in amyotrophic lateral sclerosis (ALS) and frontotemporal dementia. 52,53

Abnormal EEG and locomotor behavior of Grin2a mutant mice

To investigate effects on brain network activity, we monitored EEG in Grin2a mutant mice, analyzing signals from an electrode over the parietal cortex (Figures 7A-7E). Full details of EEG recordings in Grin2a mutant mice, including stimulus-evoked EEG measurements, are described elsewhere.⁵⁴ At 3 months of age, Grin2a+/- and Grin2a-/- mutants showed a significant increase in gamma (30-50 Hz) oscillation power during non-rapid eye movement (NREM) sleep (Figure 7A), which is reminiscent of the increase in gamma oscillations during sleep and quiet wake in SCZ patients. 55,56 Grin2a-/- also displayed elevated slow, delta, sigma, and beta oscillations relative to WTs (Figures 7B-7E). Theta and alpha oscillations were similar across all genotypes (Figures S7A and S7B).

To perform an unbiased measurement of behavioral changes, we used MoSeq, an unsupervised machine learning framework that characterizes mouse behavior by identifying sub-second behavioral motifs called syllables.⁵⁷ Both kinematic parameters (see STAR Methods) and MoSeg behavioral summaries were computed in the pipeline for each animal (Figures S7C and S7D). No significant differences were observed between Grin2a+/- mutants and their WT littermates in the tested kinematic parameters (Figures S7E-S7H). Grin2a^{-/-} mutants showed higher mean velocity than WTs (Figure S7F), but no other kinematic values were significantly different.

By sorting the behavioral syllables by their velocity and comparing usage in Grin2a mutants versus WTs, however, we noted that the highest-velocity syllables were used more by the Grin2a mutant mice as compared with WT mice (Figures 7F and 7G). These same syllables also were associated with significantly greater mean distances traveled than the remainder of the syllables (Figure 7H). Collectively, these data suggest that Grin2a mutant mice perform a subset of high velocity movements with high locomotor activity more often than their WT littermates. These behavioral patterns identified with MoSeg extend the increased baseline locomotor activity measured in AIH experiment (Figure 5N), as well as the previously reported locomotor hyperactivity of Grin2a mutant mice. 54,58,5

To further contextualize our MoSeq findings, we analyzed previously published MoSeq datasets collected from WT mice treated with antipsychotic drugs haloperidol (0.25 mg/kg) or clozapine (10 mg/kg).⁵⁷ Interestingly, the syllables with highest velocity were downregulated in mice treated with haloperidol or clozapine (Figures 7I-7K, S7I, and S7J). Thus, treatment of mice with haloperidol or clozapine results in less usage of syllables associated with high velocity movements, a behavioral pattern opposite to that observed in Grin2a mutant mice.

DISCUSSION

An animal model that has human genetics validity and that exhibits key neurobiological features of the human disease would

NeuroResource



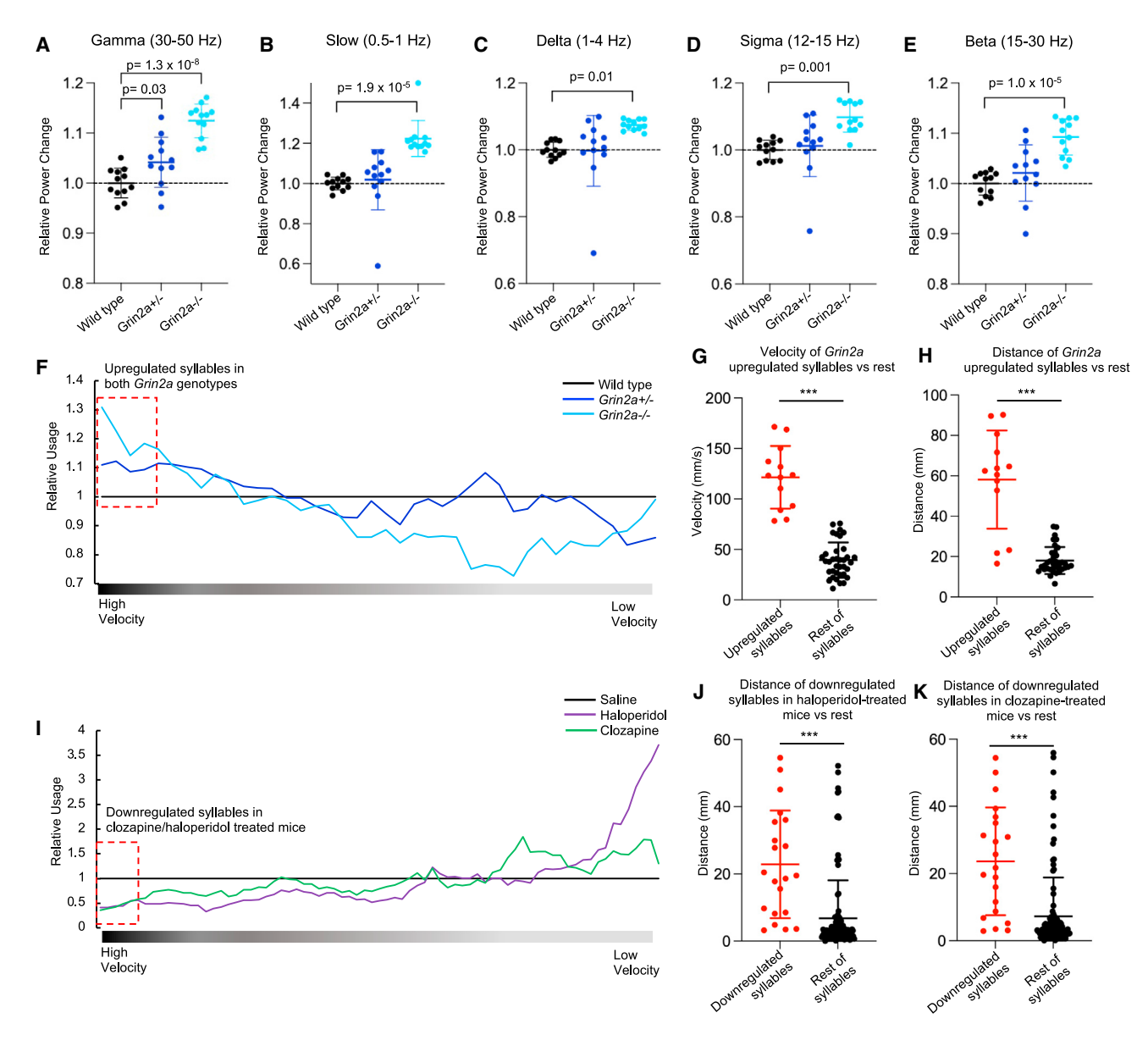


Figure 7. Abnormal EEG and locomotor behavior of Grin2a mutant mice

(A–E) Power spectral density changes in Grin2a mutants relative to wild types at ~3 months of age during NREM sleep for the indicated frequency bands (n = 12 mice/group). p values were computed using one-way ANOVAs with post hoc Tukey-Kramer tests for multiple comparisons.

(F) Relative average syllable usage in Grin2a^{+/-} and Grin2a^{-/-} normalized to wild types, after sorting the syllables by mean velocity from high to low and averaging them with a sliding window of 10 syllables. Red box indicates top quartile syllables with highest velocity.

(G and H) Mean velocity within syllables (G) and mean distance traveled during syllables (H) for top quartile syllables (red box in F) versus rest of identified syllables. (I) Relative average syllable usage in wild-type mice treated with either clozapine (10 mg/kg) or haloperidol (0.25 mg/kg), normalized to saline-treated mice after sorting the syllables by mean velocity from high to low and averaging them with a sliding window of 10 syllables. Red box indicates top quartile syllables with highest velocity. (J and K) Mean distance traveled during downregulated syllables in haloperidol- (J) and clozapine- (K) treated mice (red box in I) versus rest of identified syllables. For (I)–(K), data are taken from Wiltschko et al. 57 In (A–E), (G), (H), (J), and (K) data are shown as mean ± standard error. Asterisks (*) indicate statistical significance assessed using non-parametric ± permutation tests (see STAR Methods); ***p < 0.001. See also Figure S7.

have a transformative impact on the mechanistic understanding of SCZ. Heterozygous LoF mutations that strongly elevate the SCZ risk in humans, such as those in GRIN2A,4 offer the opportunity to create such models through heterozygous disruption of the gene in mice and other animals. Here, studying the heterozygous Grin2a mutant mouse at multiple levels, and with multiomics approaches, we made a series of discoveries that open new windows into SCZ mechanisms.

First, even though both Grin2a and Grin2b encode subunits of NMDARs, the transcriptomic changes in Grin2a+/- brain were



Neuron NeuroResource

poorly or even anti-correlated with the same brain region in Grin2b+/C456Y mice (Figures 1H-1L). The distinct global transcriptomic changes are consistent with Grin2a and Grin2b having nonidentical spatiotemporal expression patterns in the brain and different disease associations: GRIN2A but not GRIN2B is associated with SCZ. 4,60 We also noted that in contrast to Grin2b+/C456Y mutants, Grin2a+/- mutants show bigger transcriptomic changes at 12 weeks than at 4 weeks of age (Figure 1B), especially in the striatum, a period of brain maturation that might be relevant to the typical adolescence/young adult onset of SCZ.

Second, Grin2a+/- mice show surprisingly large changes in transcriptomic and proteomic phenotype, comparable to, and sometimes even greater than, Grin2a-/- mutants. Moreover, loss of just one copy of Grin2a is sufficient to cause behavioral change (hyperactivity in MoSeq and increased sensitivity to amphetamine) and neurophysiological abnormality (elevated gamma oscillation power on EEG), which are features of human SCZ and/or pharmacological models of SCZ.5

Third, Grin2a LoF has markedly different effects on different brain regions, exemplified by opposite-direction changes in synapse-related GO terms in the striatum versus the PFC and hippocampus (Figure 2A). It is also remarkable that transcriptomic measures of neuronal activity (activity-regulated gene set) and neuronal metabolism (OXPHOS/mitochondrial respiration, ribosomes), which were correlated with each other within brain regions, moved in opposite directions in different brain regions. Activity-, OXPHOS-, and ribosome-related gene sets were consistently and robustly downregulated specifically in the PFC in Grin2a^{+/-} mice, whereas these same GO terms were upregulated in the striatum and hippocampus (Figures 4A and 4C). A brain region involved in higher cognitive functions, the PFC has been much studied in relation to cognitive impairment in SCZ. 25,62 In this context, it is interesting that Grin2a+/- impacts the PFC much more than heterozygous LoF of Grin2b (Figure 1H), which is consistent with a recent human brain transcriptomic study showing that ASD has relatively little effect on PFC compared with other neocortical areas. 63 Our finding, based on transcriptomics, that Grin2a+/- mutants exhibit PFC hypofunction is intriguing because there is clinical evidence for reduced activity and brain volume in parts of PFC in SCZ.64,65 Further correlating with our RNA-seq observations, SCZ patients show hyperactivity in the hippocampus, 66-71 which correlates with symptoms of psychosis. 72 An important caveat is that we are inferring neuronal activity changes from transcriptomic alterations, so more functional measurements of neuronal activity (and energy metabolism and protein translation) in different brain regions will be critical to understand the pathophysiology of Grin2a mutant mice.

Fourth, among many pathway changes observed, perhaps most impactful is that Grin2a+/- mice show evidence of hyperdopaminergic signaling in the striatum and PFC. GO terms related to dopamine response and signaling were upregulated in pyramidal neurons of the PFC and SPNs of the striatum, while levels of Comt mRNA and protein fell. Increased dopamine release has been observed in the PFC and striatum following treatment with NMDAR antagonists. 73,74 A hyperdopaminergic state of the striatum has been reported in SCZ patients, 75-77 possibly driven by increased activity in hippocampal efferents.⁷⁸ Hyperdopaminergic signaling has been a long-standing hypothesis for the pathophysiology of SCZ, not least because antipsychotic drugs (which show efficacy against the positive symptoms of SCZ) have antagonist activity against the D2 dopamine receptor. 79,80 In this light, it is striking that in *Grin2a*^{+/-} mice, one of the most highly induced genes in striatal SPNs was Drd2, which encodes the D2 dopamine receptor (Figure 5B). Of relevance, a recent study invoked elevated striatal dopamine as the driver of "hallucination-like percepts" in mice.81

Striatal dopamine abnormalities have been postulated to be secondary to circuit dysfunction caused by altered glutamate signaling in inhibitory neurons during early postnatal brain development.⁸² Consistent with the hyperdopaminergic state being a later secondary response, the changes in dopamine-induced gene set emerged at 4 weeks of age in the striatum of Grin2a^{+/-} mutants (Figure 5L), whereas changes in GO terms related to synapses and OXPHOS and ribosomes were already apparent at 2 weeks of age (see Table S1). Moreover, our transcriptomic data provide strong evidence that the functional state (though not the number) of inhibitory interneurons is affected by Grin2a heterozygous LoF, including alteration of OXPHOS and ribosomal GO terms in inhibitory interneurons (Figures 4A and 4B). Together, our data suggest that dopamine dysregulation in Grin2a^{+/-} mutants may be a downstream event of NMDAR hypofunction in the brain, perhaps involving both excitatory and inhibitory neuron dysfunction. Although the mechanistic link between Grin2a LoF and hyperdopaminergic drive in the striatum is not clear, it is impressive that heterozygous mutation in Grin2a, a gene that surfaced from human genetics of SCZ, marries two prevailing hypotheses of SCZ pathophysiology—the "NMDAR hypofunction" hypothesis, and the "striatal hyperdopaminergic" hypothesis. It will be important to confirm by physiology experiments whether striatal dopamine signaling is enhanced in Grin2a+/- mutant mice and whether any abnormal phenotypes (molecular or functional) can be rescued by D2 antipsychotic drugs. Also, given that *Drd2*, a bona fide drug target for SCZ. emerged as a highly changed gene from our snRNA-seq analysis of Grin2a^{+/-} mice, we are hopeful that further study of transcriptomic changes in Grin2a mutants will uncover additional novel targets for SCZ treatment.

Besides support for these existing neurotransmitter theories of SCZ, our multi-omics data also reveal unanticipated mechanisms that might contribute to SCZ pathophysiology, such as perturbations in energy metabolism and protein translation, myelination, steroid/cholesterol biosynthesis, and RNA processing, as well as the involvement of non-neuronal cells. Follow-up studies delving into these mentioned mechanisms could yield further insights into the intricate molecular underpinnings of SCZ and potentially pave the way for innovative treatments that go beyond the traditional neurotransmitter-focused approaches.

STAR*METHODS

Detailed methods are provided in the online version of this paper and include the following:

- KEY RESOURCES TABLE
- RESOURCE AVAILABILITY

NeuroResource



- Lead contact
- Materials availability
- O Data and code availability
- EXPERIMENTAL MODEL AND SUBJECT DETAILS
 - O Grin2a and Grin2b mutant mice
- METHOD DETAILS
 - O Brain perfusion and dissection
 - O RNA extraction and bulk RNA-seq library preparation
 - O Quantitative real-time PCR
 - O Nuclei extraction and snRNA-seq library preparation
 - O Purification of synaptic fraction for MS
 - Western blotting
 - O EEG implantation surgery and recording
 - Motion Sequencing (MoSeq)
 - O Amphetamine-induced hyperlocomotion
- QUANTIFICATION AND STATISCTICAL ANALYSIS
 - O Bulk RNA-seq DE analysis
 - O Single-nucleus RNA-seq analysis
 - O Pseudocell DE analysis
 - Pseudobulk DE analysis
 - Gene set enrichment analysis
 - Quantitative MS analysis
 - EEG analysis
 - O MoSeq analysis

SUPPLEMENTAL INFORMATION

Supplemental information can be found online at https://doi.org/10.1016/j.neuron.2023.08.004.

ACKNOWLEDGMENTS

We thank Charles Vanderburg for assisting with mouse brain dissection and Naeem N. Nadaf, Nicolas Lapique, and Xian Adiconis for assistance with sequencing library preparations. We thank Matthew Beck and Tyler Caron for assisting with maintaining the *Grin2a* mouse colony. We thank Kris Dickson, Dheeraj Roy, Zhanyan Fu, Kevin Mastro, Gordon Fishell, and Prabhat Kunwar for invaluable feedback. Research reported in this manuscript was supported by the Stanley Center for Psychiatric Research and the Institute for Basic Science (IBS-R002-D1 to E.K.). Z.F. was supported by an Otto Hahn Fellowship of the Max Planck Society.

AUTHOR CONTRIBUTIONS

Conceptualization, M.S. and Z.F.; software, V.G.; formal analysis, A.N., S.K.S., Z.F., S.L., S.A., L.H., and S.P.M.; investigation, Z.F., N.S., K. Brenner, B.D., S.A., L.H., K. Bonanno, W.S., K.J.S., and S.P.M.; resources, E.K. and J.Q.P.; data curation, A.N.; writing – original draft, Z.F., A.N., and M.S., with inputs from all co-authors; writing – review & editing, Z.F. and M.S.; visualization, Z.F., A.N., and B.J.S.; supervision, M.S., Z.F., J.Z.L., S.K.S., B.D., S.A.C., H.K., J.Q.P., E.Z.M., S.R.D., and E.K.; funding acquisition, M.S.

DECLARATION OF INTERESTS

M.S. is cofounder and SAB member of Neumora Therapeutics and serves on the SAB of Biogen, ArcLight, Vanqua Bio, and Proximity Therapeutics. M.S. is on the advisory board of *Neuron*. S.A.C. is a member of the scientific advisory boards of Kymera, PTM BioLabs, Seer, and PrognomIQ.

Received: December 14, 2022 Revised: May 19, 2023 Accepted: August 4, 2023 Published: August 31, 2023

REFERENCES

- Sullivan, P.F., Kendler, K.S., and Neale, M.C. (2003). Schizophrenia as a complex trait: evidence from a meta-analysis of twin studies. Arch. Gen. Psychiatry 60, 1187–1192. https://doi.org/10.1001/archpsyc.60. 12.1187.
- Owen, M.J., Sawa, A., and Mortensen, P.B. (2016). Schizophrenia. Lancet 388, 86–97. https://doi.org/10.1016/S0140-6736(15)01121-6.
- Trubetskoy, V., Pardiñas, A.F., Qi, T., Panagiotaropoulou, G., Awasthi, S., Bigdeli, T.B., Bryois, J., Chen, C.Y., Dennison, C.A., Hall, L.S., et al. (2022). Mapping genomic loci implicates genes and synaptic biology in schizophrenia. Nature 604, 502–508. https://doi.org/10.1038/s41586-022-04434-5.
- Singh, T., Poterba, T., Curtis, D., Akil, H., Al Eissa, M., Barchas, J.D., Bass, N., Bigdeli, T.B., Breen, G., Bromet, E.J., et al. (2022). Rare coding variants in ten genes confer substantial risk for schizophrenia. Nature 604, 509–516. https://doi.org/10.1038/s41586-022-04556-w.
- Genovese, G., Fromer, M., Stahl, E.A., Ruderfer, D.M., Chambert, K., Landén, M., Moran, J.L., Purcell, S.M., Sklar, P., Sullivan, P.F., et al. (2016). Increased burden of ultra-rare protein-altering variants among 4,877 individuals with schizophrenia. Nat. Neurosci. 19, 1433–1441. https://doi.org/10.1038/nn.4402.
- Singh, T., Walters, J.T.R., Johnstone, M., Curtis, D., Suvisaari, J., Torniainen, M., Rees, E., Iyegbe, C., Blackwood, D., McIntosh, A.M., et al. (2017). The contribution of rare variants to risk of schizophrenia in individuals with and without intellectual disability. Nat. Genet. 49, 1167–1173. https://doi.org/10.1038/ng.3903.
- Rivas, M.A., Pirinen, M., Conrad, D.F., Lek, M., Tsang, E.K., Karczewski, K.J., Maller, J.B., Kukurba, K.R., DeLuca, D.S., Fromer, M., et al. (2015). Human genomics. Effect of predicted protein-truncating genetic variants on the human transcriptome. Science 348, 666–669. https://doi.org/10. 1126/science.1261877.
- Endele, S., Rosenberger, G., Geider, K., Popp, B., Tamer, C., Stefanova, I., Milh, M., Kortüm, F., Fritsch, A., Pientka, F.K., et al. (2010). Mutations in GRIN2A and GRIN2B encoding regulatory subunits of NMDA receptors cause variable neurodevelopmental phenotypes. Nat. Genet. 42, 1021– 1026. https://doi.org/10.1038/ng.677.
- Lesca, G., Rudolf, G., Bruneau, N., Lozovaya, N., Labalme, A., Boutry-Kryza, N., Salmi, M., Tsintsadze, T., Addis, L., Motte, J., et al. (2013). GRIN2A mutations in acquired epileptic aphasia and related childhood focal epilepsies and encephalopathies with speech and language dysfunction. Nat. Genet. 45, 1061–1066. https://doi.org/10.1038/ ng.2726.
- Pierson, T.M., Yuan, H., Marsh, E.D., Fuentes-Fajardo, K., Adams, D.R., Markello, T., Golas, G., Simeonov, D.R., Holloman, C., Tankovic, A., et al. (2014). GRIN2A mutation and early-onset epileptic encephalopathy: personalized therapy with memantine. Ann. Clin. Transl. Neurol. 1, 190–198. https://doi.org/10.1002/acn3.39.
- Strehlow, V., Heyne, H.O., Vlaskamp, D.R.M., Marwick, K.F.M., Rudolf, G., de Bellescize, J., Biskup, S., Brilstra, E.H., Brouwer, O.F., Callenbach, P.M.C., et al. (2019). GRIN2A-related disorders: genotype and functional consequence predict phenotype. Brain 142, 80–92. https://doi.org/10.1093/brain/awy304.
- Shepard, N., Baez-Nieto, D., Iqbal, S., Campbell, A.J., Pan, J.Q., Sheng, M., and Farsi, Z. (2023). Functional analysis of human GRIN2A mutations associated with schizophrenia and neurodevelopmental disorders reveals distinct pathological mechanism. bioRxiv. https://doi.org/10. 1101/2023.08.02.551645.
- Chen, W., Tankovic, A., Burger, P.B., Kusumoto, H., Traynelis, S.F., and Yuan, H. (2017). Functional evaluation of a de novo GRIN2A mutation identified in a patient with profound global developmental delay and refractory epilepsy. Mol. Pharmacol. 91, 317–330. https://doi.org/10. 1124/mol.116.106781.



Neuron NeuroResource

- 14. Yuan, H., Hansen, K.B., Zhang, J., Pierson, T.M., Markello, T.C., Fajardo, K.V., Holloman, C.M., Golas, G., Adams, D.R., Boerkoel, C.F., et al. (2014). Functional analysis of a de novo GRIN2A missense mutation associated with early-onset epileptic encephalopathy. Nat. Commun. 5, 3251. https://doi.org/10.1038/ncomms4251.
- 15. Moghaddam, B., and Javitt, D. (2012). From revolution to evolution: the glutamate hypothesis of schizophrenia and its implication for treatment. Neuropsychopharmacology 37, 4–15. https://doi.org/10.1038/npp.
- 16. Sheng, M., Cummings, J., Roldan, L.A., Jan, Y.N., and Jan, L.Y. (1994). Changing subunit composition of heteromeric NMDA receptors during development of rat cortex. Nature 368, 144-147. https://doi.org/10. 1038/368144a0.
- 17. Paoletti, P., Bellone, C., and Zhou, Q. (2013). NMDA receptor subunit diversity: impact on receptor properties, synaptic plasticity and disease. Nat. Rev. Neurosci. 14, 383-400. https://doi.org/10.1038/nrn3504.
- 18. Hall, J., and Bray, N.J. (2022). Schizophrenia genomics: convergence on synaptic development, adult synaptic plasticity, or both? Biol. Psychiatry 91, 709-717. https://doi.org/10.1016/j.biopsych.2021.10.018.
- 19. Hall, J., Trent, S., Thomas, K.L., O'Donovan, M.C., and Owen, M.J. (2015). Genetic risk for schizophrenia: convergence on synaptic pathways involved in plasticity. Biol. Psychiatry 77, 52-58. https://doi.org/ 10.1016/j.biopsych.2014.07.011.
- 20. Farsi, Z., and Sheng, M. (2023). Molecular mechanisms of schizophrenia: insights from human genetics. Curr. Opin. Neurobiol. 81, 102731.
- 21. Gandal, M.J., Zhang, P., Hadjimichael, E., Walker, R.L., Chen, C., Liu, S., Won, H., van Bakel, H., Varghese, M., Wang, Y., et al. (2018). Transcriptome-wide isoform-level dysregulation in ASD, schizophrenia, and bipolar disorder. Science 362, eaat8127. https://doi.org/10.1126/ science.aat8127.
- 22. Ruzicka, B., Mohammadi, S., Davila-Velderrain, J., Subburaju, S., Tso, R., Hourihan, M., and Kellis, M. (2021). Single-cell dissection of schizophrenia reveals neurodevelopmental-synaptic link and transcriptional resilience associated cellular state. Biol. Psychiatry 89, S106.
- 23. Kadotani, H., Hirano, T., Masugi, M., Nakamura, K., Nakao, K., Katsuki, M., and Nakanishi, S. (1996). Motor discoordination results from combined gene disruption of the NMDA receptor NR2A and NR2C subunits, but not from single disruption of the NR2A or NR2C subunit. J. Neurosci. 16. 7859-7867.
- 24. Shin, W., Kim, K., Serraz, B., Cho, Y.S., Kim, D., Kang, M., Lee, E.J., Lee, H., Bae, Y.C., Paoletti, P., and Kim, E. (2020). Early correction of synaptic long-term depression improves abnormal anxiety-like behavior in adult GluN2B-C456Y-mutant mice. PLoS Biol. 18, e3000717. https://doi.org/ 10.1371/journal.pbio.3000717.
- 25. Sakurai, T., Gamo, N.J., Hikida, T., Kim, S.H., Murai, T., Tomoda, T., and Sawa, A. (2015). Converging models of schizophrenia-Network alterations of prefrontal cortex underlying cognitive impairments. Prog. Neurobiol. 134, 178-201. https://doi.org/10.1016/j.pneurobio.2015. 09.010
- 26. Subramanian, A., Tamayo, P., Mootha, V.K., Mukherjee, S., Ebert, B.L., Gillette, M.A., Paulovich, A., Pomeroy, S.L., Golub, T.R., Lander, E.S., and Mesirov, J.P. (2005). Gene set enrichment analysis: a knowledgebased approach for interpreting genome-wide expression profiles. Proc. Natl. Acad. Sci. USA 102, 15545-15550. https://doi.org/10.1073/ pnas.0506580102.
- 27. Korotkevich, G., Sukhov, V., Budin, N., Shpak, B., Artyomov, M.N., and Sergushichev, A. (2021). Fast gene set enrichment analysis. https://doi. org/10.1101/060012.
- 28. Aryal, S., Bonanno, K., Song, B., Mani, D.R., Keshishian, H., Carr, S.A., Sheng, M., and Dejanovic, B. (2023). Deep proteomics identifies shared molecular pathway alterations in synapses of patients with schizophrenia and bipolar disorder and mouse model. Cell Rep. 42, 112497. https://doi. org/10.1016/j.celrep.2023.112497.

- 29. Koopmans, F., van Nierop, P., Andres-Alonso, M., Byrnes, A., Cijsouw, T., Coba, M.P., Cornelisse, L.N., Farrell, R.J., Goldschmidt, H.L., Howrigan, D.P., et al. (2019). Syngo: an evidence-based, expert-curated knowledge base for the synapse. Neuron 103, 217-234.e4. https://doi. org/10.1016/j.neuron.2019.05.002.
- 30. Buniello, A., MacArthur, J.A.L., Cerezo, M., Harris, L.W., Hayhurst, J., Malangone, C., McMahon, A., Morales, J., Mountjoy, E., Sollis, E., et al. (2019). The NHGRI-EBI GWAS Catalog of published genomewide association studies, targeted arrays and summary statistics 2019. Nucleic Acids Res. 47, D1005-D1012. https://doi.org/10.1093/nar/ akv1120.
- 31. Kaplanis, J., Samocha, K.E., Wiel, L., Zhang, Z., Arvai, K.J., Eberhardt, R.Y., Gallone, G., Lelieveld, S.H., Martin, H.C., McRae, J.F., et al. (2020). Evidence for 28 genetic disorders discovered by combining healthcare and research data. Nature 586, 757-762. https://doi.org/10. 1038/s41586-020-2832-5.
- 32. Satterstrom, F.K., Kosmicki, J.A., Wang, J., Breen, M.S., De Rubeis, S., An, J.Y., Peng, M., Collins, R., Grove, J., Klei, L., et al. (2020). Large-scale exome sequencing study implicates both developmental and functional changes in the neurobiology of autism. Cell 180, 568-584.e23. https:// doi.org/10.1016/j.cell.2019.12.036.
- 33. International League Against Epilepsy Consortium on Complex Epilepsies (2018). Genome-wide mega-analysis identifies 16 loci and highlights diverse biological mechanisms in the common epilepsies. Nat. Commun. 9, 5269. https://doi.org/10.1038/s41467-018-07524-z.
- 34. Cross-Disorder Group of the Psychiatric; Genomics Consortium (2019). Genomic relationships, novel loci, and pleiotropic mechanisms across eight psychiatric disorders. Cell 179, 1469-1482.e11. https://doi.org/ 10.1016/j.cell.2019.11.020.
- 35. Palmer, D.S., Howrigan, D.P., Chapman, S.B., Adolfsson, R., Bass, N., Blackwood, D., Boks, M.P.M., Chen, C.Y., Churchhouse, C., Corvin, A.P., et al. (2022). Exome sequencing in bipolar disorder identifies AKAP11 as a risk gene shared with schizophrenia. Nat. Genet. 54, 541-547. https://doi.org/10.1038/s41588-022-01034-x.
- 36. Gazestani, V., Kamath, T., Nadaf, N.M., Burris, S.J., Rooney, B., Junkkari, A., Vanderburg, C., Rauramaa, T., Therrien, M., Tegtmeyer, M., et al. (2023). Early Alzheimer's disease pathology in human cortex is associated with a transient phase of distinct cell states. https://doi. org/10.1101/2023.06.03.543569.
- 37. Robinson, M.D., McCarthy, D.J., and Smyth, G.K. (2010). edgeR: a Bioconductor package for differential expression analysis of digital gene expression data. Bioinformatics 26, 139-140. https://doi.org/10. 1093/bioinformatics/btp616.
- 38. Tremblay, R., Lee, S., and Rudy, B. (2016). GABAergic interneurons in the neocortex: from cellular properties to circuits. Neuron 91, 260-292. https://doi.org/10.1016/j.neuron.2016.06.033.
- 39. Hökfelt, T., Broberger, C., Xu, Z.Q., Sergeyev, V., Ubink, R., and Diez, M. (2000). Neuropeptides-an overview. Neuropharmacology 39, 1337-1356. https://doi.org/10.1016/s0028-3908(00)00010-1.
- 40. Tyssowski, K.M., DeStefino, N.R., Cho, J.H., Dunn, C.J., Poston, R.G., Carty, C.E., Jones, R.D., Chang, S.M., Romeo, P., Wurzelmann, M.K., et al. (2018). Different neuronal activity patterns induce different gene expression programs. Neuron 98, 530-546.e11. https://doi.org/10. 1016/i.neuron.2018.04.001.
- 41. Butovsky, O., and Weiner, H.L. (2018). Microglial signatures and their role in health and disease. Nat. Rev. Neurosci. 19, 622-635. https://doi.org/ 10.1038/s41583-018-0057-5.
- 42. Goudriaan, A., de Leeuw, C., Ripke, S., Hultman, C.M., Sklar, P., Sullivan, P.F., Smit, A.B., Posthuma, D., and Verheijen, M.H. (2014). Specific glial functions contribute to schizophrenia susceptibility. Schizophr. Bull. 40, 925-935. https://doi.org/10.1093/schbul/sbt109.
- 43. Andersson, M., Konradi, C., and Cenci, M.A. (2001). cAMP response element-binding protein is required for dopamine-dependent gene

NeuroResource



- expression in the intact but not the dopamine-denervated striatum. J. Neurosci. 21, 9930-9943.
- 44. Zhang, X., Odom, D.T., Koo, S.H., Conkright, M.D., Canettieri, G., Best, J., Chen, H., Jenner, R., Herbolsheimer, E., Jacobsen, E., et al. (2005). Genome-wide analysis of cAMP-response element binding protein occupancy, phosphorylation, and target gene activation in human tissues. Proc. Natl. Acad. Sci. USA 102, 4459-4464. https://doi.org/10.1073/ pnas.0501076102.
- 45. Savell, K.E., Tuscher, J.J., Zipperly, M.E., Duke, C.G., Phillips, R.A., 3rd, Bauman, A.J., Thukral, S., Sultan, F.A., Goska, N.A., lanov, L., and Day, J.J. (2020). A dopamine-induced gene expression signature regulates neuronal function and cocaine response. Sci. Adv. 6, eaba4221. https://doi.org/10.1126/sciadv.aba4221.
- 46. Simonetti, M., Paldy, E., Njoo, C., Bali, K.K., Worzfeld, T., Pitzer, C., Kuner, T., Offermanns, S., Mauceri, D., and Kuner, R. (2021). The impact of semaphorin 4C/Plexin-B2 signaling on fear memory via remodeling of neuronal and synaptic morphology. Mol. Psychiatry 26, 1376-1398. https://doi.org/10.1038/s41380-019-0491-4.
- 47. O'Connor, T.P., Cockburn, K., Wang, W., Tapia, L., Currie, E., and Bamji, S.X. (2009). Semaphorin 5B mediates synapse elimination in hippocampal neurons. Neural Dev. 4, 18. https://doi.org/10.1186/1749-8104-4-18.
- 48. Uesaka, N., Uchiqashima, M., Mikuni, T., Nakazawa, T., Nakao, H., Hirai, H., Aiba, A., Watanabe, M., and Kano, M. (2014). Retrograde semaphorin signaling regulates synapse elimination in the developing mouse brain. Science 344, 1020-1023. https://doi.org/10.1126/science.1252514.
- 49. Eastwood, S.L., Law, A.J., Everall, I.P., and Harrison, P.J. (2003). The axonal chemorepellant semaphorin 3A is increased in the cerebellum in schizophrenia and may contribute to its synaptic pathology. Mol. Psychiatry 8, 148-155. https://doi.org/10.1038/sj.mp.4001233.
- 50. Zhou, K., Yang, Y., Gao, L., He, G., Li, W., Tang, K., Ji, B., Zhang, M., Li, Y., Yang, J., et al. (2012). NMDA receptor hypofunction induces dysfunctions of energy metabolism and semaphorin signaling in rats: a synaptic proteome study. Schizophr. Bull. 38, 579-591. https://doi.org/10.1093/ schbul/sba132.
- 51. Fox, A.H., and Lamond, A.I. (2010). Paraspeckles. Cold Spring Harb. Perspect. Biol. 2, a000687. https://doi.org/10.1101/cshperspect.
- 52. Lim, Y.W., James, D., Huang, J., and Lee, M. (2020). The emerging role of the RNA-binding protein SFPQ in neuronal function and neurodegeneration. Int. J. Mol. Sci. 21, 7151. https://doi.org/10.3390/ijms21197151.
- 53. Lester, E., Ooi, F.K., Bakkar, N., Ayers, J., Woerman, A.L., Wheeler, J., Bowser, R., Carlson, G.A., Prusiner, S.B., and Parker, R. (2021). Tau aggregates are RNA-protein assemblies that mislocalize multiple nuclear speckle components. Neuron 109, 1675-1691.e9. https://doi.org/10. 1016/j.neuron.2021.03.026.
- 54. Herzog, L.E., Wang, L., Yu, E., Choi, S., Farsi, Z., Song, B.J., Pan, J.Q., and Sheng, M. (2023). Mouse mutants in schizophrenia risk genes GRIN2A and AKAP11 show EEG abnormalities in common with schizophrenia patients. Transl. Psychiatry 13, 92. https://doi.org/10.1038/ s41398-023-02393-7.
- 55. Tanaka-Koshiyama, K., Koshiyama, D., Miyakoshi, M., Joshi, Y.B., Molina, J.L., Sprock, J., Braff, D.L., and Light, G.A. (2020). Abnormal spontaneous gamma power is associated with verbal learning and memory dysfunction in schizophrenia. Front. Psychiatry 11, 832. https://doi. org/10.3389/fpsyt.2020.00832.
- 56. Tekell, J.L., Hoffmann, R., Hendrickse, W., Greene, R.W., Rush, A.J., and Armitage, R. (2005). High frequency EEG activity during sleep: characteristics in schizophrenia and depression. Clin. EEG Neurosci. 36, 25-35. https://doi.org/10.1177/155005940503600107.
- 57. Wiltschko, A.B., Tsukahara, T., Zeine, A., Anyoha, R., Gillis, W.F., Markowitz, J.E., Peterson, R.E., Katon, J., Johnson, M.J., and Datta, S.R. (2020). Revealing the structure of pharmacobehavioral space through motion sequencing. Nat. Neurosci. 23, 1433-1443. https://doi. org/10.1038/s41593-020-00706-3.

- 58. Hanson, J.E., Ma, K., Elstrott, J., Weber, M., Saillet, S., Khan, A.S., Simms, J., Liu, B., Kim, T.A., Yu, G.Q., et al. (2020). GluN2A NMDA receptor enhancement improves brain oscillations, synchrony, and cognitive functions in Dravet syndrome and Alzheimer's disease models. Cell Rep. 30, 381-396.e4. https://doi.org/10.1016/j.celrep.2019.12.030.
- 59. Boyce-Rustay, J.M., and Holmes, A. (2006). Genetic inactivation of the NMDA receptor NR2A subunit has anxiolytic- and antidepressant-like effects in mice. Neuropsychopharmacology 31, 2405-2414. https://doi. org/10.1038/sj.npp.1301039.
- 60. Platzer, K., Yuan, H., Schütz, H., Winschel, A., Chen, W., Hu, C., Kusumoto, H., Heyne, H.O., Helbig, K.L., Tang, S., et al. (2017). GRIN2B encephalopathy: novel findings on phenotype, variant clustering, functional consequences and treatment aspects. J. Med. Genet. 54, 460-470. https://doi.org/10.1136/jmedgenet-2016-104509.
- 61. van den Buuse, M. (2010). Modeling the positive symptoms of schizophrenia in genetically modified mice: pharmacology and methodology aspects. Schizophr. Bull. 36, 246-270. https://doi.org/10.1093/schbul/ sbp132.
- 62. Sigurdsson, T., Stark, K.L., Karayiorgou, M., Gogos, J.A., and Gordon, J.A. (2010). Impaired hippocampal-prefrontal synchrony in a genetic mouse model of schizophrenia. Nature 464, 763-767. https://doi.org/ 10.1038/nature08855
- 63. Gandal, M.J., Haney, J.R., Wamsley, B., Yap, C.X., Parhami, S., Emani, P.S., Chang, N., Chen, G.T., Hoftman, G.D., de Alba, D., et al. (2022). Broad transcriptomic dysregulation occurs across the cerebral cortex in ASD. Nature 611, 532-539. https://doi.org/10.1038/s41586-022-
- 64. Minzenberg, M.J., Laird, A.R., Thelen, S., Carter, C.S., and Glahn, D.C. (2009). Meta-analysis of 41 functional neuroimaging studies of executive function in schizophrenia. Arch. Gen. Psychiatry 66, 811-822. https://doi. org/10.1001/archgenpsychiatry.2009.91.
- 65. Pomarol-Clotet, E., Canales-Rodríguez, E.J., Salvador, R., Sarró, S., Gomar, J.J., Vila, F., Ortiz-Gil, J., Iturria-Medina, Y., Capdevila, A., and McKenna, P.J. (2010). Medial prefrontal cortex pathology in schizophrenia as revealed by convergent findings from multimodal imaging. Mol. Psychiatry 15, 823-830. https://doi.org/10.1038/mp.2009.146.
- 66. Schobel, S.A., Chaudhury, N.H., Khan, U.A., Paniagua, B., Styner, M.A., Asllani, I., Inbar, B.P., Corcoran, C.M., Lieberman, J.A., Moore, H., and Small, S.A. (2013). Imaging patients with psychosis and a mouse model establishes a spreading pattern of hippocampal dysfunction and implicates glutamate as a driver. Neuron 78, 81-93. https://doi.org/10.1016/
- 67. Talati, P., Rane, S., Kose, S., Blackford, J.U., Gore, J., Donahue, M.J., and Heckers, S. (2014), Increased hippocampal CA1 cerebral blood volume in schizophrenia. NeuroImage Clin. 5, 359–364. https://doi.org/10. 1016/j.nicl.2014.07.004.
- 68. Tregellas, J.R., Smucny, J., Harris, J.G., Olincy, A., Maharajh, K., Kronberg, E., Eichman, L.C., Lyons, E., and Freedman, R. (2014). Intrinsic hippocampal activity as a biomarker for cognition and symptoms in schizophrenia. Am. J. Psychiatry 171, 549-556. https://doi.org/ 10.1176/appi.ajp.2013.13070981.
- 69. Tregellas, J.R., Ellis, J., Shatti, S., Du, Y.P., and Rojas, D.C. (2009). Increased hippocampal, thalamic, and prefrontal hemodynamic response to an urban noise stimulus in schizophrenia. Am. J. Psychiatry 166, 354–360. https://doi.org/10.1176/appi.ajp.2008.
- 70. Holt, D.J., Weiss, A.P., Rauch, S.L., Wright, C.I., Zalesak, M., Goff, D.C., Ditman, T., Welsh, R.C., and Heckers, S. (2005). Sustained activation of the hippocampus in response to fearful faces in schizophrenia. Biol. Psychiatry 57, 1011–1019. https://doi.org/10.1016/j.biopsych.2005. 01.033.
- 71. Malaspina, D., Storer, S., Furman, V., Esser, P., Printz, D., Berman, A., Lignelli, A., Gorman, J., and Van Heertum, R. (1999). SPECT study of



Neuron NeuroResource

- visual fixation in schizophrenia and comparison subjects. Biol. Psychiatry 46, 89-93. https://doi.org/10.1016/s0006-3223(98)00306-0.
- 72. Silbersweig, D.A., Stern, E., Frith, C., Cahill, C., Holmes, A., Grootoonk, S., Seaward, J., McKenna, P., Chua, S.E., and Schnorr, L. (1995). A functional neuroanatomy of hallucinations in schizophrenia. Nature 378, 176-179. https://doi.org/10.1038/378176a0.
- 73. Löscher, W., Annies, R., and Hönack, D. (1991). The N-methyl-Daspartate receptor antagonist MK-801 induces increases in dopamine and serotonin metabolism in several brain regions of rats. Neurosci. Lett. 128, 191-194. https://doi.org/10.1016/0304-3940(91)90258-u.
- 74. Moghaddam, B., Adams, B., Verma, A., and Daly, D. (1997). Activation of glutamatergic neurotransmission by ketamine: a novel step in the pathway from NMDA receptor blockade to dopaminergic and cognitive disruptions associated with the prefrontal cortex. J. Neurosci. 17, 2921-2927
- 75. Grace, A.A. (2016). Dysregulation of the dopamine system in the pathophysiology of schizophrenia and depression. Nat. Rev. Neurosci. 17, 524-532. https://doi.org/10.1038/nrn.2016.57.
- 76. Laruelle, M., Abi-Dargham, A., Gil, R., Kegeles, L., and Innis, R. (1999). Increased dopamine transmission in schizophrenia: relationship to illness phases. Biol. Psychiatry 46, 56-72. https://doi.org/10.1016/s0006-3223(99)00067-0.
- 77. Laruelle, M., and Abi-Dargham, A. (1999). Dopamine as the wind of the psychotic fire: new evidence from brain imaging studies. Psychopharmacol. 13, 358-371. https://doi.org/10.1177/ 026988119901300405
- 78. Stone, J.M., Howes, O.D., Egerton, A., Kambeitz, J., Allen, P., Lythgoe, D.J., O'Gorman, R.L., McLean, M.A., Barker, G.J., and McGuire, P. (2010). Altered relationship between hippocampal glutamate levels and striatal dopamine function in subjects at ultra high risk of psychosis. Biol. Psychiatry 68, 599-602. https://doi.org/10.1016/j.biopsych.2010. 05.034.
- 79. Kapur, S., and Mamo, D. (2003). Half a century of antipsychotics and still a central role for dopamine D2 receptors. Prog. Neuropsychopharmacol. Biol. Psychiatry 27, 1081-1090. https://doi.org/10.1016/j.pnpbp.2003. 09 004
- 80. Meltzer, H.Y., Li, Z., Kaneda, Y., and Ichikawa, J. (2003). Serotonin receptors: their key role in drugs to treat schizophrenia. Prog. Neuropsychopharmacol. Biol. Psychiatry 27, 1159-1172. https://doi. org/10.1016/j.pnpbp.2003.09.010.
- 81. Schmack, K., Bosc, M., Ott, T., Sturgill, J.F., and Kepecs, A. (2021). Striatal dopamine mediates hallucination-like perception in mice. Science 372, eabf4740. https://doi.org/10.1126/science.abf4740.
- 82. Nakazawa, K., and Sapkota, K. (2020). The origin of NMDA receptor hypofunction in schizophrenia. Pharmacol. Ther. 205, 107426. https://doi. org/10.1016/j.pharmthera.2019.107426.
- 83. Fleming, S.J., Chaffin, M.D., Arduini, A., A., A., Banks, E., Marioni, J.C., Philippakis, A.A., Ellinor, P.T., and Babadi, M. (2019). Unsupervised removal of systematic background noise from droplet-based singlecell experiments using CellBender. https://doi.org/10.1101/791699.
- 84. Li, B., and Dewey, C.N. (2011). RSEM: accurate transcript quantification from RNA-Seq data with or without a reference genome. BMC Bioinformatics 12, 323. https://doi.org/10.1186/1471-2105-12-323.
- 85. Love, M.I., Huber, W., and Anders, S. (2014). Moderated estimation of fold change and dispersion for RNA-seq data with DESeq2. Genome Biol. 15, 550. https://doi.org/10.1186/s13059-014-0550-8.
- 86. Stuart, T., Butler, A., Hoffman, P., Hafemeister, C., Papalexi, E., Mauck, W.M., 3rd, Hao, Y., Stoeckius, M., Smibert, P., and Satija, R. (2019). Comprehensive integration of single-cell data. Cell 177, 1888-1902.e21. https://doi.org/10.1016/j.cell.2019.05.031.
- 87. Wolock, S.L., Lopez, R., and Klein, A.M. (2019). Scrublet: computational identification of cell doublets in single-cell transcriptomic data. Cell Syst. 8, 281-291.e9. https://doi.org/10.1016/j.cels.2018.11.005.

- 88. Hao, Y., Hao, S., Andersen-Nissen, E., Mauck, W.M., 3rd, Zheng, S., Butler, A., Lee, M.J., Wilk, A.J., Darby, C., Zager, M., et al. (2021). Integrated analysis of multimodal single-cell data. Cell 184, 3573-3587.e29. https://doi.org/10.1016/j.cell.2021.04.048.
- 89. Phipson, B., Sim, C.B., Porrello, E.R., Hewitt, A.W., Powell, J., and Oshlack, A. (2022). Propeller: testing for differences in cell type proportions in single cell data. Bioinformatics 38, 4720-4726. https://doi.org/ 10.1093/bioinformatics/btac582.
- 90. Harris, C.R., Millman, K.J., van der Walt, S.J., Gommers, R., Virtanen, P., Cournapeau, D., Wieser, E., Taylor, J., Berg, S., Smith, N.J., et al. (2020). Array programming with NumPy. Nature 585, 357-362. https://doi.org/ 10.1038/s41586-020-2649-2.
- 91. McKinney, W. (2010). Data structures for statistical computing in Python. In Proceedings of the Python in Science Conference, pp. 56-61.
- 92. Virtanen, P., Gommers, R., Oliphant, T.E., Haberland, M., Reddy, T., Cournapeau, D., Burovski, E., Peterson, P., Weckesser, W., Bright, J., et al. (2020). SciPy 1.0: fundamental algorithms for scientific computing in Python. Nat. Methods 17, 261-272. https://doi.org/10.1038/s41592-019-0686-2
- 93. Hunter, J.D. (2007). Matplotlib: A 2D graphics environment. Comput. Sci. Eng. 9, 90-95. https://doi.org/10.1109/MCSE.2007.55
- 94. Yao, Z., van Velthoven, C.T.J., Nguyen, T.N., Goldy, J., Sedeno-Cortes, A.E., Baftizadeh, F., Bertagnolli, D., Casper, T., Chiang, M., Crichton, K., et al. (2021). A taxonomy of transcriptomic cell types across the isocortex and hippocampal formation. Cell 184, 3222-3241.e26. https://doi.org/ 10.1016/j.cell.2021.04.021.
- 95. Saunders, A., Macosko, E.Z., Wysoker, A., Goldman, M., Krienen, F.M., de Rivera, H., Bien, E., Baum, M., Bortolin, L., Wang, S., et al. (2018). Molecular diversity and specializations among the cells of the adult mouse brain. Cell 174, 1015-1030.e16. https://doi.org/10.1016/j.cell. 2018.07.028.
- 96. Yao, Z., Liu, H., Xie, F., Fischer, S., Adkins, R.S., Aldridge, A.I., Ament, S.A., Bartlett, A., Behrens, M.M., Van den Berge, K., et al. (2021). A transcriptomic and epigenomic cell atlas of the mouse primary motor cortex. Nature 598, 103-110. https://doi.org/10.1038/s41586-021-03500-8.
- 97. Biancalani, T., Scalia, G., Buffoni, L., Avasthi, R., Lu, Z., Sanger, A., Tokcan, N., Vanderburg, C.R., Segerstolpe, A., Zhang, M., et al. (2021). Deep learning and alignment of spatially resolved single-cell transcriptomes with Tangram. Nat. Methods 18, 1352-1362. https://doi.org/10. 1038/s41592-021-01264-7.
- 98. Dejanovic, B., Huntley, M.A., De Mazière, A., Meilandt, W.J., Wu, T., Srinivasan, K., Jiang, Z., Gandham, V., Friedman, B.A., Ngu, H., et al. (2018). Changes in the synaptic proteome in tauopathy and rescue of tau-induced synapse loss by C1q antibodies. Neuron 100, 1322-1336.e7. https://doi.org/10.1016/j.neuron.2018.10.014.
- 99. Dejanovic, B., Wu, T., Tsai, M.C., Graykowski, D., Gandham, V.D., Rose, C.M., Bakalarski, C.E., Ngu, H., Wang, Y., Pandey, S., et al. (2022). Complement C1q-dependent excitatory and inhibitory synapse elimination by astrocytes and microglia in Alzheimer's disease mouse models. Nat. Aging 2, 837-850.
- 100. Zheng, G.X., Terry, J.M., Belgrader, P., Ryvkin, P., Bent, Z.W., Wilson, R., Ziraldo, S.B., Wheeler, T.D., McDermott, G.P., Zhu, J., et al. (2017). Massively parallel digital transcriptional profiling of single cells. Nat. Commun. 8, 14049. https://doi.org/10.1038/ncomms14049.
- 101. Ding, J., Adiconis, X., Simmons, S.K., Kowalczyk, M.S., Hession, C.C., Marjanovic, N.D., Hughes, T.K., Wadsworth, M.H., Burks, T., Nguyen, L.T., et al. (2020). Systematic comparison of single-cell and single-nucleus RNA-sequencing methods. Nat. Biotechnol. 38, 737-746. https:// doi.org/10.1038/s41587-020-0465-8.
- 102. Zeisel, A., Hochgerner, H., Lönnerberg, P., Johnsson, A., Memic, F., van der Zwan, J., Häring, M., Braun, E., Borm, L.E., La Manno, G., et al. (2018). Molecular architecture of the mouse nervous system. Cell 174, 999-1014.e22. https://doi.org/10.1016/j.cell.2018.06.021.

Neuron

NeuroResource



- 103. Kanton, S., Boyle, M.J., He, Z., Santel, M., Weigert, A., Sanchís-Calleja, F., Guijarro, P., Sidow, L., Fleck, J.S., Han, D., et al. (2019). Organoid single-cell genomic atlas uncovers human-specific features of brain development. Nature 574, 418-422. https://doi.org/10.1038/s41586-019-1654-9.
- 104. Cao, J., Cusanovich, D.A., Ramani, V., Aghamirzaie, D., Pliner, H.A., Hill, A.J., Daza, R.M., McFaline-Figueroa, J.L., Packer, J.S., Christiansen, L., et al. (2018). Joint profiling of chromatin accessibility and gene expression in thousands of single cells. Science 361, 1380-1385. https://doi. org/10.1126/science.aau0730.
- 105. van Dijk, D., Sharma, R., Nainys, J., Yim, K., Kathail, P., Carr, A.J., Burdziak, C., Moon, K.R., Chaffer, C.L., Pattabiraman, D., et al. (2018). Recovering gene interactions from single-cell data using data diffusion. Cell 174, 716-729.e27. https://doi.org/10.1016/j.cell.2018.05.061.
- 106. Law, C.W., Chen, Y., Shi, W., and Smyth, G.K. (2014). voom: Precision weights unlock linear model analysis tools for RNA-seq read counts. Genome Biol. 15, R29. https://doi.org/10.1186/gb-2014-15-2-r29.
- 107. Lun, A.T.L., and Marioni, J.C. (2017). Overcoming confounding plate effects in differential expression analyses of single-cell RNA-seq data. Biostatistics 18, 451–464. https://doi.org/10.1093/biostatistics/kxw055.
- 108. Levy, D.R., Hunter, N., Lin, S., Robinson, E.M., Gillis, W., Conlin, E.B., Anyoha, R., Shansky, R.M., and Datta, S.R. (2023). Mouse spontaneous behavior reflects individual variation rather than estrous state. Curr. Biol. 33, 1358-1364.e4. https://doi.org/10.1016/j.cub.2023.02.035.
- 109. Lin, S., Gillis, W.F., Weinreb, C., Zeine, A., Jones, S.C., Robinson, E.M., Markowitz, J., and Datta, S.R. (2022). Characterizing the structure of mouse behavior using motion sequencing. https://doi.org/10.48550/ arXiv.2211.08497.





STAR***METHODS**

KEY RESOURCES TABLE

REAGENT or RESOURCE	SOURCE	IDENTIFIER
Antibodies		
Mouse anti-COMT	BD Biosciences	Cat# 611970; RRID: AB_399391
Rabbit anti-GluN1	Cell Signaling	Cat# 5704; RRID: AB_1904067
Rabbit anti-GluN2A	Cell Signaling	Cat# 4205; RRID: AB_2112295
Rabbit anti-HOMER1	Synaptic Systems	Cat# 160 003; RRID: AB_887730
Rabbit anti-HOMER3	Synaptic Systems	Cat# 160 303; RRID: AB_10804288
Mouse anti-Psd95	BioLegend	Cat# 810401; RRID: AB_2564750
Mouse anti-β-ACTIN, HRP conjugated	Sigma Aldrich	Cat# A3854; RRID: AB_262011
Experimental models: Organisms/strains		
Mouse: B6;129S-Grin2a <tm1nak></tm1nak>	RIKEN BioResource Research Center	RRID: IMSR_RBRC02256
Mouse: Grin2b+/C456Y mutant mice	Shin et al. ²⁴	N/A
Mouse: C57/BL6J	Jackson Laboratories	RRID:IMSR_JAX:000664
Critical commercial assays		
RNeasy Mini Kit	Qiagen	Cat# 74106
TruSeq Stranded mRNA Kit	Illumina	Cat# 20020595
TaqMan RNA-to-CT 1-Step Kit	Thermo Fisher	Cat# 4392653
NextGEM SC 3' LibGel v3.1 Kit	10x Genomics	Cat# 1000268
Dual Index Kit TT Set A	10x Genomics	Cat# 1000215
Sera-Mag™ Magnetic carboxylate modified particles	Cytiva	Cat# 24152105050250
TMTpro™ 16plex Label Reagent Set	Thermo Fisher	Cat#A44520
Sep-Pak tC18 1cc vac cartridge, 50mg	Waters Corp.	Cat#WAT054960
Zorbax 300Extend-C18 columns (2.1mm ID x 250mm length, 4.6mm ID x 250mm length)	Agilent	Cat#899999-555 (custom order)
75 μm ID picofrit column	Thermo Scientific	Cat#PF360-75-10-N-5
Reprosil C18-AQ 1.9 µm beads	Dr Maisch GmbH	Cat#r119.aq.003
Deposited data		
Raw and processed bulk and single-nucleus RNA-seq data	This paper	GEO: GSE218573
Processed single-nucleus RNA-seq data	This paper	scPortal: https://singlecell.broadinstitute.org/ single_cell?scpbr=grin2a-mutant-mice
Analyzed DE and GSEA data	This paper	Tables S1 and S3–S6; Mendeley data: https://doi.org/10.17632/d5t8dtnmx4.1
Original mass spectra	This paper	http://massive.ucsd.edu Username: MSV000090487 Password: astrocytes
Post-MoSeq behavioral database	This paper	https://zenodo.org/record/8180752
All original code	This paper	DESeq, EdgeR Pseudobulk, MoSeq: https://github.com/aanicolella/Farsi_et_al_2023 Pseudocell: https://app.terra.bio/#workspaces/ fbrihuman/sconline_integrative_analysis
Oligonucleotides		<u> </u>
TaqMan gene expression assay-Grin2a	Thermo Fisher	Cat#4331182 Mm00433802_m1
TaqMan gene expression assay-Grin2b	Thermo Fisher	Cat# 4331182 Mm00433820_m1

NeuroResource



Continued		
REAGENT or RESOURCE	SOURCE	IDENTIFIER
TaqMan gene expression assay-Akap13	Thermo Fisher	Cat# 4351372 Mm01320098_m1
TaqMan gene expression assay-Comt	Thermo Fisher	Cat# 4331182 Mm00514377_m1
TaqMan gene expression assay-Npy	Thermo Fisher	Cat# 4331182 Mm01410146_m1
TaqMan gene expression assay-Bsn	Thermo Fisher	Cat# 4331182 Mm00464452_m1
TaqMan gene expression assay-Actb	Thermo Fisher	Cat# 4331182 Mm02619580_g1
TaqMan gene expression assay-Gapdh	Thermo Fisher	Cat# 4331182 Mm99999915_g1
Software and algorithms		
Motion Sequencing	The Datta Lab	https://www.moseq4all.org
CellRanger v3.0.2	10x Genomics	RRID: SCR_017344
CellBender v0.1.0	Fleming et al. ⁸³	https://github.com/broadinstitute/CellBender
RSEM v1.3.0	Li et al. ⁸⁴	RRID:SCR_013027
DESeq2 v1.20.0	Love et al. ⁸⁵	RRID: SCR_015687
Seurat v3.2.3	Stuart et al.86	RRID: SCR_016341
Scrublet v0.2.3	Wolock et al.87	RRID: SCR_018098
Azimuth	Hao et al. ⁸⁸	RRID: SCR_021084
Speckle v0.0.3	Phipson et al. ⁸⁹	https://github.com/phipsonlab/speckle
EdgeR v3.22.3	Robinson et al. ³⁷	RRID: SCR_012802
fGSEA v1.16.0	Korotkevich et al. ²⁷	RRID: SCR_020938
MATLAB	Mathworks	RRID: SCR_001622
R v4.1.3	The R Foundation	RRID: SCR_001905
Python v3.11.6	Python Software Foundation	RRID: SCR_008394
Numpy	Harris et al. ⁹⁰	RRID:SCR_008633
Pandas	McKinney et al. ⁹¹	RRID:SCR_018214
Scipy	Virtanen et al. 92	RRID:SCR_008058
Matplotlib	Hunter et al. ⁹³	RRID:SCR_008624
GraphPad Prism	GraphPad	RRID: SCR_002798
Spectrum Mill	Broad Institute	RRID: SCR_022171
LUNA	Harvard Medical School	http://zzz.bwh.harvard.edu/luna
Other		
Allen Brain Atlas "WHOLE CORTEX & HIPPOCAMPUS – 10X GENOMICS"	Yao et al. ⁹⁴	https://portal.brain-map.org/atlases-and-data/ rnaseq/mouse-whole-cortex-and-hippocampus-10x
DropViz "annotation.BrainCellAtlas_ Saunders_version_2018.04.01.rds"	Saunders et al. 95	http://dropviz.org/
Azimuth Mouse Motor Cortex	Yao et al. ⁹⁶	https://zenodo.org/record/4546935

RESOURCE AVAILABILITY

Lead contact

Further information and requests for resources and reagents should be directed to and will be fulfilled by the lead contact, Zohreh Farsi (zfarsi@broadinstitute.org).

Materials availability

This study did not generate any new unique reagents.

Data and code availability

• All Bulk and single-nucleus RNA-seq data have been deposited at GEO and at the Broad Single Cell Portal (scPortal) and are publicly available as of the date of publication. The original mass spectra and the protein sequence databases used for searches have been deposited in the public proteomics repository MassIVE. The post-MoSeq behavioral database have been deposited at Zenodo. Main figures, supplemental figures, supplemental tables, and full DE tables for bulk RNA-seq analysis and pseudocell analysis of snRNA-seq data are available via Mendeley Data. Accession numbers and DOIs are listed in the key resources table.





- All original code has been deposited on GitHub and Terra Workspace and is publicly available as of the date of publication. DOIs are listed in the key resources table.
- Any additional information required to reanalyze the data reported in this paper is available from the lead contact upon request.

EXPERIMENTAL MODEL AND SUBJECT DETAILS

Grin2a and Grin2b mutant mice

Grin2a-/- mice, originally generated as described,²³ were obtained from RIKEN BioResource Research Center (RBRC02256) and were crossed against wild-type C57/BL6J mice (Jackson Laboratory, #000664) to generate Grin2a+/- mice. The Grin2a+/- mice were then crossed with each other to produce Grin2a+/-, Grin2a-/- and wild-type littermates used in all the experiments. All animals were housed at AAALAC-approved facilities on a 12-hour light/dark cycle, with food and water available ad libitum. All procedures involving Grin2a mutant mice were approved by the Broad Institute IACUC (Institutional Animal Care and Use Committee) and conducted in accordance with the NIH Guide for the Care and Use of Laboratory Animals. Male Grin2a mutant mice and their wild-type littermates at 2, 4, 12 and 20 weeks of age were used for research in this study.

Frozen whole brain tissues of *Grin2b*^{+/C456Y} and their wild-type littermates, all under the genetic background of C57BL/6J, were kindly provided by Dr. Eunjoon Kim (Department of Biological Sciences, Korea Advanced Institute of Science and Technology, South Korea).

METHOD DETAILS

Brain perfusion and dissection

Brain tissues for bulk and snRNA-seq were prepared as described at protocols.io (https://www.protocols.io/view/fresh-frozenmouse-brain-preparation-for-single-nu-bcbrism6). To minimize one source of variability, only male mice were used in this study. Briefly, at 2, 4, 12 and 20 weeks of age, male *Grin2a*^{+/-}, *Grin2a*^{-/-} and wild-type mice were anesthetized by administration of isoflurane in a gas chamber. While anesthesia was prolonged via a nose cone through which 3% isoflurane flowed, transcardial perfusions were performed with ice-cold Hank's Balanced Salt Solution (HBSS) to remove blood from the brain. The brains were immediately frozen for three minutes in liquid nitrogen vapor and stored at -80 °C until dissection.

Brain dissection was performed in a cryostat (Leica CM3050S), and all the tools required for dissection were precooled to -20 °C. The cerebellum was first removed with a cut in the coronal plane using a razor blade precooled to -20 °C. The brains were then cut at the midsagittal plane to use the right and left hemispheres of each brain for bulk and snRNA-seq experiments, respectively. To dissect the prefrontal cortex, each brain hemisphere was securely mounted from lateral surface onto a cryostat chuck with O.C.T. (optimal cutting temperature) freezing medium (Tissue-Tek) such that the midsagittal surface was left exposed and thermally unperturbed. The medial prefrontal cortex was then dissected by hand in the cryostat using an ophthalmic microscalpel (Feather safety Razor no. P-715) precooled to -20 °C. To dissect the other brain regions, the remaining brain hemisphere was removed from the chuck and mounted from the olfactory bulb onto a new cryostat chuck with O.C.T. freezing medium. Coronal sections were cut by advancing the cryostat 30 µm at a time in trimming mode until the dorsal hippocampus was visible. This stepwise approach reduced disruption of the brain tissue surface that could occur with larger steps. The dorsal hippocampus was then dissected by hand using the ophthalmic microscalpel, and the thalamus was collected using a precooled biopsy punch (Thermo Fisher Scientific) with 0.15 cm diameter. 30 μm-coronal sections were further cut by advancing the cryostat until the lateral ventricles became triangle-shaped. The somatosensory cortex was then dissected by hand using the ophthalmic microscalpel and the dorsal striatum was collected using a precooled biopsy punch with 0.15 cm diameter. All the brain regions were identified according to the Allen Brain Atlas. Each excised tissue was placed into a precooled 1.5-ml PCR tube and stored at -80°C.

RNA extraction and bulk RNA-seq library preparation

RNA was prepared from micro-dissected tissues using RNeasy Mini Kit (Qiagen) following the manufacturer's instructions. Briefly, tissue samples were lysed and homogenized, placed into columns, and bound to the RNeasy silica membrane. Next, contaminants were washed away, columns were treated with DNase (Qiagen) to digest residual DNA, and concentrated RNA was eluted in water. RNA concentration was measured using a NanoDrop Spectrophotometer and RNA integrity (RIN) was measured with RNA pico chips (Agilent) using a 2100 Bioanalyzer Instrument (Agilent). Purified RNA was then stored at -80°C until library preparation for bulk RNAseq analysis.

Bulk sequencing libraries were prepared using a TruSeq Stranded mRNA Kit (Illumina) following the manufacturer's instructions. 200 ng of isolated total RNA from each sample was used and the concentration of resulting cDNA library was measured with High Sensitivity DNA chips (Agilent) using a 2100 Bioanalyzer Instrument (Agilent). A 10 nM normalized library was pooled, and sequencing was performed on a NovaSeg S2 (Illumina) with 50 bases each for reads 1 and 2 and 8 bases each for index reads 1 and 2.

Neuron

NeuroResource



Quantitative real-time PCR

RNA was extracted with the RNeasy Mini Kit (Qiagen) as stated above. Quantitative real-time PCR was performed using the TaqMan RNA-to-Ct 1-Step Kit and TaqMan gene expression assays (Thermo Fisher Scientific). PCR amplifications were performed in triplicate or quadruplicates (n = 4-5 animals per genotype) and gene expression was determined by the comparative cycle threshold ($\Delta\Delta$ Ct) method using *Gapdh* as an internal housekeeping gene control.

Nuclei extraction and snRNA-seq library preparation

Brain tissue dissection and nuclei extraction were performed on the same day to avoid freeze-thaw cycles. A gentle, detergent-based dissociation was used to extract the nuclei, according to a previously published protocol, ⁹⁷ also available at protocols.io (https://www.protocols.io/view/frozen-tissue-nuclei-extraction-bbseinbe). Extracted nuclei were then loaded into the 10x Chromium V3.1 system (10x Genomics) and library preparation was performed according to the manufacturer's protocol. A 10 nM normalized library was pooled, and sequencing was performed on a NovaSeq S2 (Illumina) with 28 and 75 bases for reads 1 and 2 and 10 bases each for index reads 1 and 2.

Purification of synaptic fraction for MS

P28-32 *Grin2a* mutant mice were sacrificed using CO₂ anesthesia, after which hippocampi were dissected rapidly, flash-frozen on dry ice, and stored at -80°C. Synapse fractions were purified as described previously. ^{98,99} Briefly, hippocampi were thawed and dounce-homogenized (10 strokes) in ice-cold homogenization buffer (5 mM HEPES pH 7.4, 1 mM MgCl₂, 0.5 mM CaCl₂, supplemented with phosphatase (Sigma 4906837001) and protease inhibitors (Sigma 4693159001)). The homogenate was centrifuged for 10 min at 1,400 g (4°C) and the resulting supernatant (S1) was re-centrifuged at 13,800 g for 10 min (4°C). The resulting pellet (P2) was resuspended in 0.32 M Sucrose, 6 mM Tris-HCl (pH 7.5) and layered gently on a 0.85 M, 1 M, 1.2 M discontinuous sucrose gradient (all layers in 6 mM Tris-HCl pH 7.5) and ultracentrifuged at 82,500 g for 2 hours (4°C). The synaptosome fraction which sediments at the 1 M and 1.2 M sucrose interface, was collected, an equal volume of ice-cold 1% Triton X-100 (in 6 mM Tris-HCl pH 7.5) was added, mixed thoroughly, and incubated on ice for 15 min. The mixture was ultracentrifuged at 32,800 g for 20 min (4°C), and the pellet (the synapse fraction) was collected by resuspension in 1% SDS. A small aliquot was taken to measure the protein concentration, and the remaining protein was stored at -80°C until being processed for mass spectrometry (MS) or Western blotting.

Sixteen synaptic fractions extracted from the hippocampus of wild type, $Grin2a^{+/-}$ and $Grin2a^{-/-}$ mouse brains were used for the proteomics study using tandem mass tag (TMT) isobaric labeling strategy for quantitation (n = 5 wild type; n = 6 $Grin2a^{+/-}$; n = 5 $Grin2a^{-/-}$). All samples contained 35 ug protein pre-digestion and were processed using the following workflow.

Samples were prepared in a one-percent SDS buffer to ensure proper dissolution of membrane proteins and digested using single-pot, solid-phase-enhanced sample-preparation (SP3) technology. Reduction of proteins using 5 mM dithiothreitol and alkylation of them using 10 mM iodoacetamide was performed at 60° C and room temperature, respectively. All samples were diluted to a total volume of 140 μ L with a working solution consisting of 50 mM HEPES, 5mM EDTA, 50 mM NaCl, 2 ug/mL aprotinin, 10 μ g/mL leupeptin, 1 mM PMSF, 10 mM NaF, 1:100 PIC2 and PIC3 and 1% SDS. The proteins were then bound to SP3 paramagnetic beads in a 1:10 protein to bead ratio using 100% ethanol to induce binding. Samples were then incubated at 24 °C for 5 min mixing at 1000 rpm and then placed on a magnetic rack to pull down the beads. Beads were kept immobilized and washed three times with 1 mL of 80% ethanol, then resuspended in 100 mM ammonium bicarbonate to maintain a 1 μ g/ μ L bead concentration. Each sample was sonicated in a water bath for 1 min and gently vortexed to homogenize. Then sequential digestion steps were performed using 1:25 enzyme to substrate ratio of Lys-C for 2 hours and Trypsin overnight at 37 °C. Following digestion, samples were centrifuged at 12,000 rpm for 5 min then placed on a magnetic rack where the supernatant was collected and acidified to a 1% final concentration of formic acid.

Post-digest peptide measurements were performed by Nanodrop Spectrophotometer (Thermo Fisher Scientific) and 30 μ g aliquots per sample were made for labeling. A TMT16 plex was constructed by randomly assigning the samples from each group to channels within the plex. Samples were reconstituted in 50 mM HEPES buffer for labeling and 20 μ L of 25 μ g/ μ L TMT16 reagent was added for the labeling reaction. After confirming successful labeling (> 95% label incorporation), the reactions were quenched with 5% hydroxylamine and combined. The mixed sample was then desalted on a 50 mg tC18 SepPak cartridge and fractionated on a 2.1 mm x 250mm Zorbax 300 extend-c18 reverse-phased column. One-minute fractions were collected during the entire elution and then concatenated into 12 fractions.

One microgram of each proteome fraction was analyzed on a QE mass spectrometer (Thermo Fisher Scientific) coupled to an easy-nLC 1200 LC system (Thermo Fisher Scientific). Samples were separated using 0.1% Formic acid/3% Acetonitrile as buffer A and 0.1% Formic acid /90% Acetonitrile as buffer B on a 27cm 75um ID picofrit column packed in-house with Reprosil C18-AQ 1.9 μ m beads (Dr Maisch GmbH) with a 90 min gradient consisting of 6-20% B in 62 min, 20-30% B for 22 min, 30-60% B in 9 min, 60-90% B for 1 min followed by a hold at 90% B for 5 min. The MS method consisted of a full MS scan at 70,000 resolution and an AGC target of 3e6 from 300-1800 m/z followed by MS2 scans collected at 35,000 resolution with an AGC target of 5e4 with a maximum injection time of 120 ms and a dynamic exclusion of 15 seconds. The isolation window used for MS2 acquisition was 0.7 m/z and 12 most abundant precursor ions were fragmented with a normalized collision energy (NCE) of 27 optimized for TMT16 data collection.





Western blotting

The protein concentrations of synaptic fractions or total brain lysate were determined using Bicinchoninic acid assay (BCA; Pierce 23227). To equalize protein concentrations, samples were diluted with 6X SDS-Sample buffer (Boston Bioproducts BP-111R; to a final concentration of 1X) and water. The diluted samples were then heated at 95°C for 5-7 min after which they were stored at -20°C until SDS-PAGE. Before running on a gel, samples were thawed, heated at 95°C for 1 min and centrifuged briefly. Equal amounts of protein in an equal volume were loaded for each sample on 4-20% Tris-glycine polyacrylamide gels; the gels were run using Tris-glycine SDS running buffer at constant voltage. Proteins were transferred to 0.2 μm Nitrocellulose membranes using semi-dry transfer (Bio-Rad Transblot Turbo; 25V 30 min). Membranes were blocked using 5% milk in Tris-buffered saline supplemented with 0.1% Tween-20 (TBST) for 1.5 hours at room-temperature (RT). Membranes were then probed overnight (4 °C) with primary antibodies (1:1000 for all antibodies) in 5% milk TBST with gentle rotation. After four 5-min washes in TBST, membranes were incubated with either 1:5,000-10,000 HRP- or Biotin-conjugated (Jackson Immunoresearch) anti-IgG antibody raised against the appropriate species in 5% TBST for 90 min (RT). The latter membranes were washed four times (5 min each, RT) vigorously in TBST and labeled further with 1:10,000 Streptavidin Poly-HRP (Pierce 21140; in 5% milk TBST at RT, 1 hour). All membranes were then washed four times in TBST and imaged on the FluorChem-E (Protein Simple) or the ChemiDoc MP (Bio-Rad) platforms. Enhanced chemiluminescence and exposures were optimized to obtain signals in the linear range. Membranes were then stripped, re-blocked with 5% milk TBST, re-probed with a different primary antibody and imaged again as described.

For validating the MS results, 1 µg protein of synaptic fraction samples were loaded in gels probing for HOMER1 and HOMER3, while 3.5 μg protein was loaded in those probing for GluN2A, GluN1, and Psd95.

For COMT, 20 μg protein total prefrontal or striatal lysates were loaded in gels.

HOMER1, HOMER3, Psd95 and COMT were probed using HRP-conjugated anti-lgG antibodies, while GluN2A and GluN1 were probed using the Biotin-Streptavidin-poly HRP approach. HOMER1, HOMER3, and GluN1 were probed on fresh membranes while Psd95, GluN2A were probed on a membrane previously probed for GluN1. β-ACTIN was probed using an HRP-conjugated primary antibody subsequent to imaging of other proteins.

The details of the primary antibodies used, and species they were raised in, are provided in the key resources table.

EEG implantation surgery and recording

6- to 9-week-old mice (n = 12 mice/group) were deeply anesthetized with isoflurane. A prefabricated EEG/EMG headmount (#8201-SS, Pinnacle Technology, Lawrence, KS) was secured to the skull with three 0.10" intracranial electrode screws (#8403, Pinnacle Technology) at the following stereotactic coordinates: parietal recording electrode (-2 AP, 1.5 ML to Bregma), ground and reference electrodes (bilaterally -1 AP, 2 ML to Lambda). The electromyogram (EMG) electrodes were placed bilaterally in the nuchal muscles. Electrodes were soldered to the EEG/EMG head-mount and dental acrylic was used to secure the connections. Animals were given at least one week of post-operative recovery before EEG recording. Following recovery from EEG implantation, mice were tethered to the Pinnacle recording system, with at least 24 hours of habituation before recording. For sleep/wake recordings, EEG/EMG signals were recorded for 24 hours from the onset of the dark phase, ZT12 (6 pm EDT or 7 pm EST). Animals remained tethered to the Pinnacle system throughout the testing period with ad libitum access to food and water. All signals were digitized at a sampling rate of 1000 Hz, filtered (1-100 Hz bandpass for EEG; 10-1 kHz bandpass for EMG), and acquired using the Sirenia Acquisition program (Pinnacle Technology). EEG recordings took place at a timepoint roughly corresponding to 3-months of age (age range: 8-10 weeks).

Motion Sequencing (MoSeq)

MoSeq open field assay (OFA) behavioral analysis was done on mouse 3D pose data recorded in the MoSeq recording apparatus. The apparatus included a black matte plastic bucket as the arena where the mouse ran and a rigid cage that enclosed the arena. A Kinect for Windows v.2 (Microsoft) depth sensing camera was stably mounted on the cage to record the mouse's behavior in 3D from a top-down view. Animals were habituated to the behavioral room in their home cage for 10 min before recording, and all MoSeq sessions were conducted during the mouse's dark cycle in a red light-lit room. Each session was recorded for 20 min at a sampling rate of 30 frames per second. Before and between each recording session, the arena was wiped down with water, then 70% ethanol, then water, and then wiped dry. 16 wild-type, 9 Grin2a+/- and 13 Grin2a-/- mice were used for MoSeq OFA recordings.

Amphetamine-induced hyperlocomotion

Dextroamphetamine sulfate was ordered from Millipore Sigma (1180004). On the day of testing, naïve 11-13 week old male Grin2a heterozygous or littermate control mice were habituated to the testing room (white lights on) in their homecages for 30 min before being weighed and randomly assigned to one of the testing groups of vehicle (0.9% sterile saline, 1.0, 2.0, or 3 mg/kg Dextroamphetamine sulfate). Dextroamphetamine sulfate was reconstituted in sterile ultra-pure water and pH'd to approximately 7.3. The doses displayed on Figure 5P are salt-corrected. After 30 min habituation to the room, animals were placed into a cleaned Omnitech Electronics Inc SuperFlex Open Field apparatus (cleaned with 70% ethanol) and allowed to freely explore the lit (white light) open field box (16inch x 16inch dimensions) for 90 min. At precisely 90 min after being placed in the open field box, the animal was briefly removed and injected subcutaneously with either vehicle or one of the three doses of Dextroamphetamine sulfate at 5 µL per gram body weight. The animal was then placed immediately back into the open field box and allowed to freely explore the box for another

Neuron

NeuroResource



90 min. At the end of the task the animal was removed, and the box was cleaned with 70% ethanol. Distance traveled in cm was measured by infrared beam brakes and was binned every 5 min. Basal locomotion was calculated from T0 min to T85 min after the mice were placed into the open field apparatus. Dextroamphetamine sulfate induced hyperlocomotion distance traveled was calculated from immediately after dosing (T90 min) to the end of the task (T180 min). The experimenter and subsequent data analysis were blinded to both the mouse genotype and to the treatment group of the animals.

QUANTIFICATION AND STATISCTICAL ANALYSIS

Bulk RNA-seq DE analysis

RSEM v1.3.0⁸⁴ was used to estimate gene and isoform level expression values for our bulk RNA-seq samples. The M25 (GRCm38.p6) GENCODE reference was generated using RSEM-prepare-reference with default parameters. Expression values were calculated using RSEM-calculate-expression with the following flags: –bowtie2, –paired-end, –estimate-rspd, –append-names, and –sort-bamby-coordinate. The DESeq2 v1.20.0⁸⁵ package was used to run DE analysis of each of the brain regions and ages. All replicates for a given age and brain region were read into a single DESeq object to ensure that normalization was consistent across all genotypes of a given comparison. Log_2Fold Change (Log_2FC) values were adjusted using DESeq2's lfcShrink function with the 'normal' shrinkage estimator. Differentially expressed genes (DEGs) were defined as genes with FDR < 0.05 and absolute value of Log_2FC > 0.2. All DEGs from bulk RNA-seq for all brain regions, ages and genotypes can be found in Table S1.

DESeq2 was also used to run DE analysis between $Grin2a^{+/-}$ (4-week and 12-week) versus $Grin2b^{+/C456Y}$ 4-week samples for each brain region. For this analysis, all heterozygous and wild-type replicates for each region were read into a DESeq object. DESeq contrasts were then used to test for differences between the $Grin2a^{+/-}$ and $Grin2b^{+/C456Y}$, taking into account the differences between batches. More formally, we considered the contrast defined by $(Grin2a^{+/-} - Grin2a^{+/+}) - (Grin2b^{+/C456Y} - Grin2b^{+/+})$. DEGs were defined as genes with FDR < 0.05 and absolute value of $Log_2FC > 0.2$.

For comparing the transcriptomic changes in $Grin2a^{+/-}$ versus $Grin2a^{-/-}$, the Pearson's correlation r values were calculated between Log_2FC values of the same brain regions in $Grin2a^{+/-}$ versus $Grin2a^{-/-}$. It should be noted that the use of the same set of wild types for $Grin2a^{+/-}$ and $Grin2a^{-/-}$ DE analysis may lead to over inflated correlation estimates.

A list of number of reads for each brain region, genotype and age has been provided in Table S1. We did not notice a strong relationship between number of DEGs and average coverage, suggesting depth of sequencing is not the main driver of variation in number of DEGs between regions.

Single-nucleus RNA-seg analysis

The Cell Ranger v3.0.2 pipeline (10x Genomics)¹⁰⁰ was used to align reads from snRNA-seq to a mm10 mouse reference genome, which was built to include introns (https://cf.10xgenomics.com/supp/cell-exp/refdata-gex-mm10-2020-A.tar.gz). The –chemistry=SC3Pv3 and –expect-cells=10000 flags were used in addition to default parameters for Cell Ranger count. Replicates for each brain region and age were down-sampled to the same number of reads per cell using Cell Ranger aggr with default parameters. Ambient RNA removal was performed on the 12-week Hippocampus CellRanger aggr output, split by replicate, using CellBender v0.1.0, with the arguments –expected-cells 10000 and –total-droplets-included 25000.⁸³ Quality control metrics for each sample used in this study may be found in Table S5.

Unique Molecular Identifier (UMI) counts were analyzed using the Seurat v3.2.3⁸⁶ package. Nuclei expressing less than 500 genes were removed and the remaining nuclei were normalized by total expression, multiplied by ten thousand, and log transformed. Seurat's ScaleData function was then used to scale the data. Linear dimension reduction by PCA was performed using Seurat's RunPCA function on the scaled data on variable genes, and significant PCs were identified. The nuclei were clustered in the PCA space using Seurat's FindNeighbors and FindClusters functions then visualized using Uniform Manifold Approximation and Projection (UMAP) using significant PCs. Doublet identification was performed using the Scrublet v0.2.3⁸⁷ Python package with default parameters. Clusters and nuclei with a scrublet score above the region-specific thresholds were determined to be doublets and were removed from the data. The table below shows the used scrublet score thresholds for all snRNA-seq datasets:

Dataset	Scrublet Score Threshold
12w-HP	0.18
12w-PFC	0.43
12w-SSC	0.40
12w-ST	0.40
12w-TH	0.40
4w-HP	0.20
4w-PFC	0.40



Cluster cell type identification was performed using the Azimuth R package. 89 The references used for each brain region are summarized in the table below:

Brain region	Azimuth Reference(s) Used
Hippocampus	Allen Brain Atlas "WHOLE CORTEX & HIPPOCAMPUS – 10X GENOMICS" 94, DropViz "annotation.BrainCellAtlas_Saunders_version_2018.04.01.rds" 95
PFC	Azimuth Mouse Motor Cortex, 96 Allen Brain Atlas "WHOLE CORTEX & HIPPOCAMPUS - 10X GENOMICS"
SSC	Azimuth Mouse Motor Cortex
Striatum	DropViz "annotation.BrainCellAtlas_Saunders_version_2018.04.01.rds", mousebrain.org "Atlas of the Adolescent Mouse Brain"
Thalamus	
	DropViz "annotation.BrainCellAtlas_Saunders_version_2018.04.01.rds". mousebrain.org "Atlas of the Adolescent Mouse Brain"

These cell type assignments were then confirmed using the region-specific cell type marker genes. Neuronal subtypes were similarly identified by re-clustering nuclei of the given major cell type and confirming the Azimuth subtype identity labels through marker gene expression. Marker genes for the more widely classified major cell types and subtypes were identified in the literature. ¹⁰¹ Seurat's FindMarkers function was used to identify marker genes for rarer cell types and subtypes. These markers were then queried on mouseBrain.org ¹⁰² and or dropviz.org ⁹⁵ to evaluate the cell type identity. A full list of the marker genes used in this study may be found in Figures S2F–S2M.

The propeller function from the speckle R v0.0.3 package⁸⁹ was used with arcsin normalization to test if there were statistical differences in major cell type and subtype composition across genotypes within each dataset.

Pseudocell DE analysis

For differential expression analysis, we employed a pseudocell approach³⁶ for each age and brain region that aggregates expression of every 40 nuclei with similar transcriptomes within each replicate, cell type, and subtype. The pseudocell method resolves known technical variation issues of snRNA-seq transcriptome data including dropout expressions and pseudoreplication through averaging expression of similar nuclei. 103,104 To construct pseudocells, single nuclei were first grouped based on replicate and cell type. Within each group, pseudocell centers were identified by applying k-means clustering on the top 30 principal components (PCs) with k set so that each cluster contains 20 nuclei at minimum and 40 nuclei on average. We also weighted PCs by their variance explained to ensure the stability of the results across different group sizes (i.e., cell types per replicate). Random walk methods are shown to have superior performance in identifying nuclei with similar transcriptome profiles compared with the spherical, distance-based methods. 86,105 Therefore, we assigned nuclei to the pseudocell centers (i.e., k-means centroids) using a random walk approach on the cell-cell distances in the PCA space. 105 Lastly, we constructed pseudocell samples by aggregating the raw UMI counts of nuclei assigned to each pseudocell. This resulted in representation of each cell type or subtype from each replicate by multiple pseudocells. Cell types and subtypes that were identified but did not have enough nuclei present to create at least two pseudocells per replicate were removed. Differential expression analysis was performed using limma's duplicateCorrelation mixed model analysis function with robust empirical Bayes moderated t-statistics and mouse ID as random effect. 106 Genotype and the percentage of mitochondrial reads were used as covariates for all analyses. Experiment batch number was added as a covariate for Grin2a 12-week hippocampus (12w-HP) and Grin2a 12-week PFC, where samples were sourced from two separate sequencing runs. Samples of each batch are indicated in Table S5.

Genes with Benjamini-Hochberg adjusted p-value of less than 0.05 and absolute $Log_2FC > 0.2$ were deemed as DEGs. To further ensure the robustness of the identified DE genes, we calculated the log fold-change pattern (summarized as up or down regulated) of every pairwise combination of experiment (either Het or KO samples) versus WT samples. For example, a total of 3 WT samples x 3 KO samples = 9 comparisons for KO and 3 WT samples x 4 Het samples = 12 comparisons for Het DE genes. As a measure of robustness, we next calculated the fraction of comparisons in which the log fold-change had a similar direction to that of the mixed linear model. We observed this measure of robustness is above 0.8 for the majority ($\sim 60\%$) of the DEGs, indicating that the fold-change pattern of DEGs is shared across samples rather than being driven by a subset. We retained DEGs with robustness score above 0.8 as DEGs. A list of all DEGs for all cell types, brain regions and ages from pseudocell analysis can be found in Table S5.

The clusters that were identified in the initial clustering for each brain region but removed for the pseudocell analysis due to low nuclei counts are as follows: **Hippocampus (4- and 12-week)**: Cajal Retzius, Endothelial, Ependyma, SST Chodl inhibitory subtype; **PFC (4- and 12-week)** and **SSC (12-week)**: Endothelial, Vascular, SST Chodl inhibitory subtype, L6b excitatory subtype (additionally, L5/6 NP excitatory subtype was removed from 12-week SSC); **Striatum (12-week)**: Choroid Plexus, Endothelial, Vascular, the cholinergic Interneuron_Chat subtype; **Thalamus (12-week)**: Endothelial, Ependyma, Vascular.

Neuron

NeuroResource



Pseudobulk DE analysis

We also utilized a pseudobulk approach ¹⁰⁷ for differential expression analysis. For this analysis, counts were grouped by cell type and replicate. All gene counts were summed across each replicate within each cell type, resulting in one count value per replicate per cell type. Differential expression analysis was then run using the EdgeR v3.22.3 R package.³⁷ Experiment batch number was added as a covariate for *Grin2a* 12w-HP and *Grin2a* 12w-PFC, where samples were sourced from two separate sequencing runs. Genes with Benjamini-Hochberg adjusted p-value of less than 0.05 were deemed as DEGs. A list of all DEGs for all cell types, brain regions and ages from EdgeR analysis can be found in Table S3.

Gene set enrichment analysis

The DESeq2 t-stat values from bulk RNA-seq analysis or the Log₂FC values from pseudocell or EdgeR analysis were extracted to run Gene Set Enrichment Analysis (GSEA)²⁶ using the fGSEA v1.16.0 package²⁷ and either the C5 v7.2 gene set collection (including 14,765 Gene Ontology (GO) terms) from Molecular Signature Database (http://www.gsea-msigdb.org/gsea/msigdb), SynGO collection²⁹ or gene sets generated from the literature (Table S2). For proteomics data, proteins were pre-ranked using their moderated t-statistic within each comparison (*Grin2a*+/- vs wild type or *Grin2a*-/- vs wild type). For proteins with multiple isoforms, the isoform with the largest number of spectra was used for pre-ranking. For each of these gene sets, mouse gene symbols from transcriptomics and proteomics results were mapped to matching *Homo sapiens* homolog-associated gene symbols through annotations extracted from Ensembl's BioMart data service; the human symbols were then used to perform GSEA. A list of all significant GO terms (FDR < 0.05) for all datasets are provided in the following tables: Bulk RNA-seq (Table S1); snRNA-seq EdgeR analysis (Table S4); snRNA-seq pseudocell analysis (Table S6); proteomics (Table S7).

For the 'activity regulated' gene-set, the neuronal activity-induced rapid, delayed and slow primary response genes defined by Tyssowski et al. 40 were compiled. For the 'Dopamine-induced' gene-set, genes with FDR < 0.1 that were upregulated in striatal neuronal culture following one hour dopamine treatment 45 were used. The "cAMP-induced CREB target' gene-set was identified by Zhang et al. 44 For a list of curated gene-sets please see Table S2.

Quantitative MS analysis

The data was searched on Spectrum Mill MS Proteomics Software (Broad Institute) using mouse database that contained 47,069 entrees downloaded from Uniprot.org on 12/28/2017. The Spectrum Mill generated proteome level export which was filtered for proteins identified by two or more peptides for further analysis. Protein quantification was achieved by taking the ratio of TMT reporter ions for each sample the median of all channels. TMT16 reporter ion intensities were corrected for isotopic impurities in the Spectrum Mill protein/peptide summary module using the afRICA correction method which implements determinant calculations according to Cramer's Rule and correction factors obtained from the reagent manufacturer's certificate of analysis (https://www.thermofisher.com/order/catalog/product/90406) for lot number VA299611.

After performing median-MAD normalization, a moderated two-sample t-test was applied to the datasets to compare wild-type, $Grin2a^{+/-}$ and $Grin2a^{-/-}$ sample groups. Significant differentially expressed proteins (DEPs) were defined as proteins with nominal p-value < 0.05 and absolute value of $Log_2FC > 0.2$. A list of all DEPs for $Grin2a^{+/-}$ and $Grin2a^{-/-}$ hippocampal samples are provided in Table S7.

EEG analysis

Sleep state classification (NREM, REM or Wake) was performed on 10 second epochs of EEG/EMG data using a machine learning model as described previously. ⁵⁴ LUNA software for EEG analysis (http://zzz.bwh.harvard.edu/luna) was used to compute absolute power for each oscillatory band (slow: 0.5-1 Hz, delta: 1-4 Hz, theta: 4-8 Hz, alpha: 8-12 Hz, sigma: 12-15 Hz, beta: 15-30 Hz, gamma: 30-50 Hz) for NREM sleep during the light cycle, where mice are predominantly asleep. Statistical differences between wild type, $Grin2a^{+/-}$ and $Grin2a^{-/-}$ animals were computed using one-way ANOVAs with post hoc Tukey-Kramer tests for multiple comparisons using MATLAB (MathWorks, Natick, MA, RRID: SCR_001622).

MoSeq analysis

The depth videos were processed in the extraction pipeline as described previously. 57,108,109 The kinematic values such as velocity, angle, the position of the mouse's centroid, position to center, length, height, and width were extracted from the videos. The depth images were cropped to 80 pixels by 80 pixels and processed such that the mouse center was at the frame center and the nose was always pointing right. The extracted frames went through principal component analysis to reduce the dimensionality and the top 10 principal components (PCs) were input into a MoSeq autoregressive hierarchical Dirichlet process hidden Markov model (AR-HMM) to segment the depth videos into modulated sub-second behavioral motifs, called syllables. The model was trained in robust mode, such that the noise of the syllables in AR-HMM follows a t-distribution. The model self-transition bias parameter that controlled the average syllable durations, kappa, was selected after scanning through a range of kappa values. The syllable duration distributions in the models trained with different kappa values were compared with the block duration distributions from a model-free changepoint detection model. The kappa value that yielded a syllable duration median that best matched that of the model-free block duration was selected for training the final models. The final models with the kappa found in kappa scan (kappa = 1149215) trained with 1,000 iterations of Gibbs sampling and the model that had the median log likelihood was selected for further data analysis. The final single





model included all 16 wild-type, 9 Grin2a+/- and 13 Grin2a-/- mice in the MoSeq open field assay recordings. The model fitting yielded 49 syllables that explains 99% of the total frames.

Two sessions were filtered out in the behavioral analysis due to abnormal mouse sizes. The behavioral summaries of an example wild-type mouse were computed from a 5 min segment in the middle of the example session. The speed was calculated as the absolute 2D distance traveled between two frames divided by 1/30 second (depth video sampling frame rate 30 fps). The length was computed as the length of the mouse body contour in each frame. The distance to center was computed as the magnitude of the centroid of the animal to the center of the detected region of interest (ROI) that represented the arena, normalized by the radius

Syllable usages are computed from syllable orders within each session and normalized within each group. Differences between the mean velocity and distance traveled between two groups are done with Welch's t-test from scipy.stats.ttest_ind with equal_var=False, and permutation test. In the permutation test, the number of permutations is 99999 and 1 pseudo count is added in computing p value.

For the clozapine (10 mg/kg) or haloperidol (0.25 mg/kg) analysis, we used publicly available MoSeq model syllable label results at https://github.com/dattalab/moseq-drugs. The modeling procedures were described in detail in Wiltschko et al. b and the data was recorded using Kinect for Windows v.1 instead of Kinect for Windows v.2 in this experiment.

Supplemental information

Brain-region-specific changes in neurons and glia and dysregulation of dopamine signaling

in Grin2a mutant mice

Zohreh Farsi, Ally Nicolella, Sean K. Simmons, Sameer Aryal, Nate Shepard, Kira Brenner, Sherry Lin, Linnea Herzog, Sean P. Moran, Katherine J. Stalnaker, Wangyong Shin, Vahid Gazestani, Bryan J. Song, Kevin Bonanno, Hasmik Keshishian, Steven A. Carr, Jen Q. Pan, Evan Z. Macosko, Sandeep Robert Datta, Borislav Dejanovic, Eunjoon Kim, Joshua Z. Levin, and Morgan Sheng

FIGURE S1

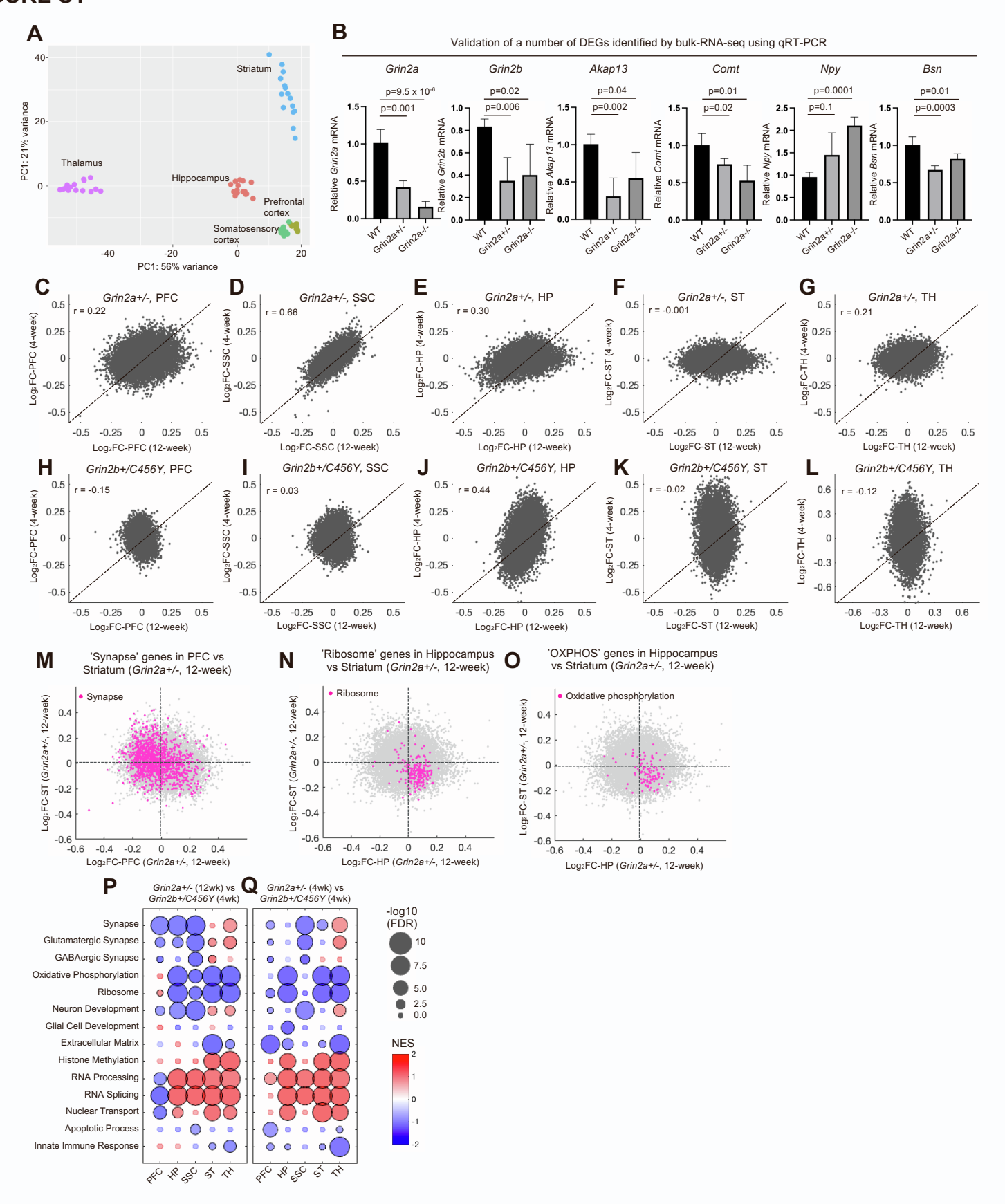


Figure S1. Age- and brain region-specific transcriptomic changes in *Grin2a* and *Grin2b* mutant mice, Related to Figure 1 and 2.

- (A) PCA plot showing the clustering of brain regions from 4-week *Grin2a* mutant animals and their wild-type littermates. Each circle represents one animal (n = 5 per genotype). PC, principal component.
- (**B**) Comparison of relative mRNA level measured by qRT-PCR (normalized to *Gapdh* mRNA) for several DEGs identified in the hippocampus of 12-week *Grin2a*^{+/-} animals. Data are shown as mean +/- standard error (n = 4-5 biological replicates). WT, wild type; p values are computed using two-tailed Student's t test.
- (**C-L**) Gene expression correlation at 12 weeks versus 4 weeks in five tested brain regions in $Grin2a^{+/-}$ (**C-G**), and in $Grin2b^{+/C456Y}$ (**H-L**). Pearson's r correlation values are indicated on the plots.
- (**M-O**) Transcriptomic changes in the PFC (**M**) and hippocampus (**N-O**) versus the striatum in 12-week *Grin2a*^{+/-} highlighting genes in the 'Synapse' (**M**), 'Ribosome' (**N**) and 'Oxidative phosphorylation' (OXPHOS) (**O**) GO terms.
- (**P-Q**) GSEA results for the studied brain regions using DE results from $Grin2a^{+/-}$ (12-week) versus $Grin2b^{+/C456Y}$ (4-week) comparison (**P**) and from $Grin2a^{+/-}$ (4-week) versus $Grin2b^{+/C456Y}$ (4-week) comparison (**Q**), showing enrichment pattern for a selection of GO terms from MSigDB. Circles with black outlines indicate statistical significance (FDR < 0.05).

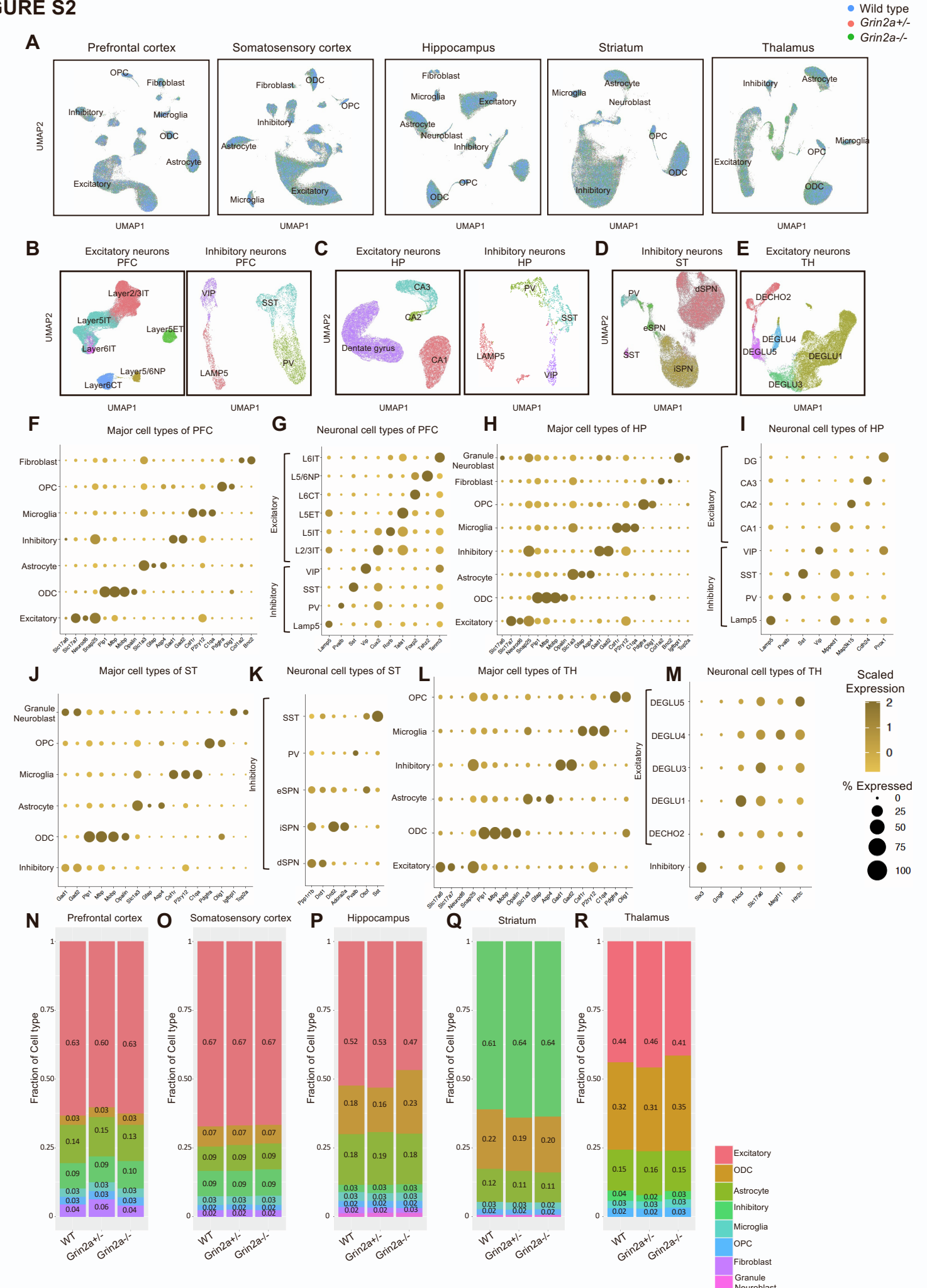


Figure S2. Diverse cell types were identified by snRNA-seq analysis in different brain regions of *Grin2a* mutant mice, Related to Figure 3.

- (A) UMAP representation of major cell types identified in five brain regions in 12-week *Grin2a* animals. Nuclei are colored based on their genotype.
- (**B-E**) UMAP representation of excitatory and inhibitory neuron subtypes identified in the PFC (similar neuronal subtypes were identified in the SSC) (**B**), hippocampus (**C**), striatum (**D**) and thalamus (**E**) in 12-week *Grin2a* animals. Similar subtypes were identified in the PFC and hippocampus in 4-week *Grin2a* animals.
- (**F-M**) Dot plots showing the scaled expression (measured in transcripts per 10K over all nuclei) and percent of cells expressing marker genes of each cell type identified in the PFC (**F-G**), hippocampus (**H-I**), striatum (**J-K**) and thalamus (**L-M**) in 12-week *Grin2a* animals. Similar marker genes as in **F-I** were used to identify different cell types in 12-week SSC and 4-week PFC and in 4-week hippocampus datasets.
- (N-R) Fraction of each identified cell type in the PFC (N), SSC (O), hippocampus (P), striatum (Q) and thalamus (R) in 12-week Grin2a animals. Each column represents the average values for one genotype (n = 4-6 animals per genotype). No significant difference was observed in the proportion of identified cell types between Grin2a mutant mice and their wild-type littermates (see Methods).

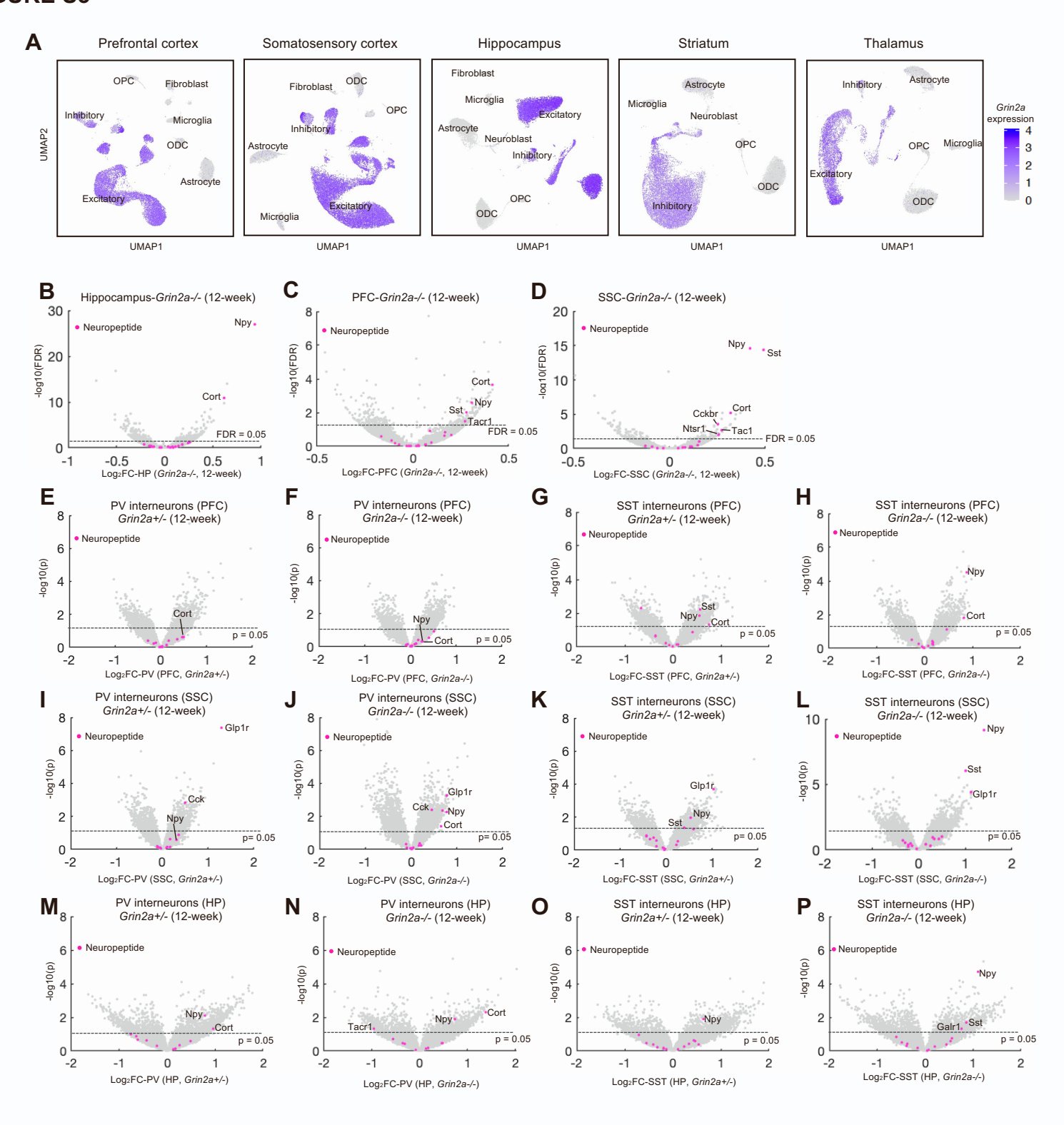


Figure S3. Changes in expression of neuropeptide genes in inhibitory neurons of cortex and hippocampus in 12-week *Grin2a* mutant mice, Related to Figure 3.

- (A) UMAP representation of the major cell types identified in five brain regions in 12-week *Grin2a* animals. Nuclei are colored based on *Grin2a* expression.
- (**B-D**) Volcano plots of transcriptomic changes in bulk RNA-seq data from hippocampus (**B**), PFC (**C**), and SSC (**D**) in 12-week *Grin2a*^{-/-} highlighting genes from the 'neuropeptides and their receptors' gene-set (Table S2).
- (**E-P**) Volcano plots of transcriptomic changes in PV (**E-F**) and SST (**G-H**) interneuron of PFC, PV (**I-J**) and SST (**K-L**) interneuron of SSC, and PV (**M-N**) and SST (**O-P**) interneuron of hippocampus in 12-week *Grin2a*^{+/-} and *Grin2a*^{-/-} highlighting genes from the 'neuropeptides and their receptors' gene-set (Table S2).

Figure S4. Changes in activity-, metabolism-, and cholesterol-related pathways in neuronal and non-neuronal cells in different brain regions of *Grin2a*^{-/-} mice, Related to Figure 4.

- (**A-B**) GSEA results from the 5 major cell types across brain regions in 12-week (**A**) and neuronal subtypes in 4-week (**B**) *Grin2a*^{-/-} mutant mice.
- (**C**) Volcano plot of transcriptomic changes in excitatory neurons of PFC in 12-week *Grin2a*^{+/-} highlighting genes from the 'Oxidative phosphorylation' (OXPHOS) GO term.
- (**D**) Transcriptomic changes in layer 2/3IT excitatory neurons of PFC in 4-week *Grin2a^{+/-}* versus *Grin2a^{-/-}* highlighting genes in the 'Ribosome' GO terms.
- (**E-F**) Volcano plots of transcriptomic changes in bulk RNA-seq data from the PFC (**E**) and striatum (**F**) in 12-week *Grin2a*^{+/-} highlighting genes from the 'activity regulated' gene-set (Table S2).
- (**G**) Enrichment of activity-regulated gene-set in the studied brain regions (bulk RNA-seq) in $Grin2a^{-/-}$ at 4 and 12 weeks.
- (H-I) GSEA results using GO terms related to cholesterol biosynthesis in excitatory subtypes, inhibitory neurons, astrocytes, and oligodendrocytes (ODCs) of the studied brain regions in 12-week (I) *Grin2a*^{-/-} mutant mice.
- (**J**) Volcano plots of transcriptomic changes in astrocytes of PFC, SSC, hippocampus, and striatum in 12-week *Grin2a*^{-/-} highlighting genes from the 'Regulation of cholesterol biosynthetic process' GO term.
- (**K**) Transcriptomic changes in hippocampal astrocytes in *Grin2a*^{+/-} at 12 weeks versus *Grin2a*^{+/-} at 4 weeks highlighting genes from the 'Regulation of cholesterol biosynthetic process' GO term. In all the bubble plots circles with black outlines indicate statistical significance (FDR < 0.05).

FIGURE S5

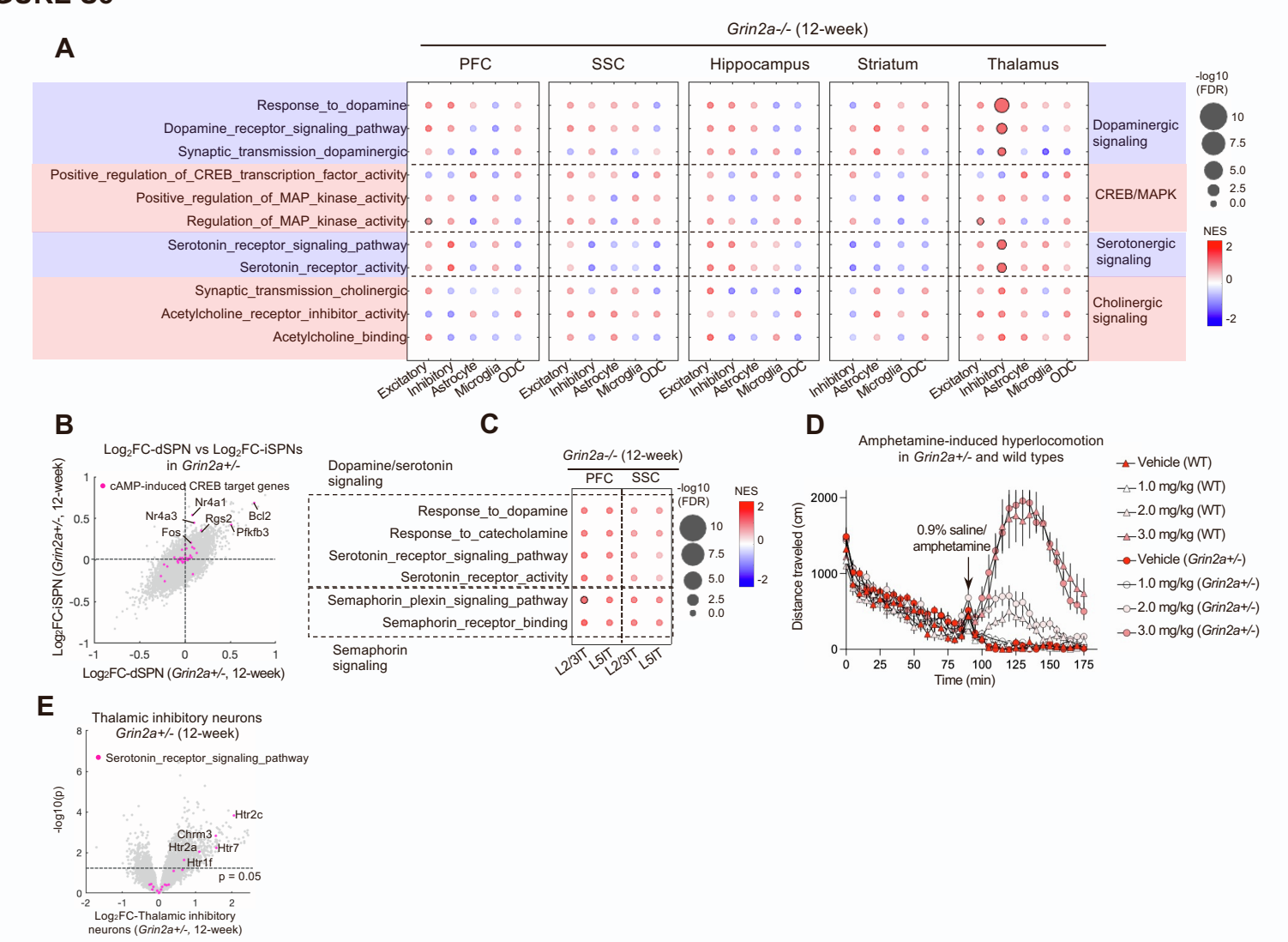


Figure S5. Hypersensitivity to amphetamine and increased serotonergic signaling in the thalamus of *Grin2a*^{+/-} mice, Related to Figure 5.

- (A) GSEA results from the 5 major cell types across brain regions in 12-week *Grin2a*^{-/-} mutant mice.
- (**B**) Transcriptomic changes in dSPNs versus iSPNs in the striatum of 12-week *Grin2a*^{+/-} highlighting the cAMP-induced CREB target genes (Table S2).
- (**C**) Changes in serotonin, dopamine and semaphorin signaling GO terms in layer 2/3IT and layer 5IT in PFC and SSC at 12 weeks in *Grin2a*-/-.
- (**D**) Locomotion traces of wild-type and $Grin2a^{+/-}$ mice before and after saline/amphetamine administration. Wild-type/ $Grin2a^{+/-}$ mice were placed in the locomotion box and allowed to freely explore for 90 min. At 90 min (indicated by the black arrow), the animals were quickly removed from the box and dosed with either 0.9% saline or 1, 2, or 3 mg/kg of amphetamine subcutaneously and immediately placed back in the box to freely explore for another 90 min. Distance traveled is binned into 5 min bins. Data are shown as mean +/- standard error of mean (n = 7-9) wild types per amphetamine dose; n = 10 $Grin2a^{+/-}$ per amphetamine dose).
- (E) Volcano plot of transcriptomic changes in inhibitory neurons of thalamus in 12-week *Grin2a*+/- highlighting genes from the 'Serotonin receptor signaling pathway' GO term.

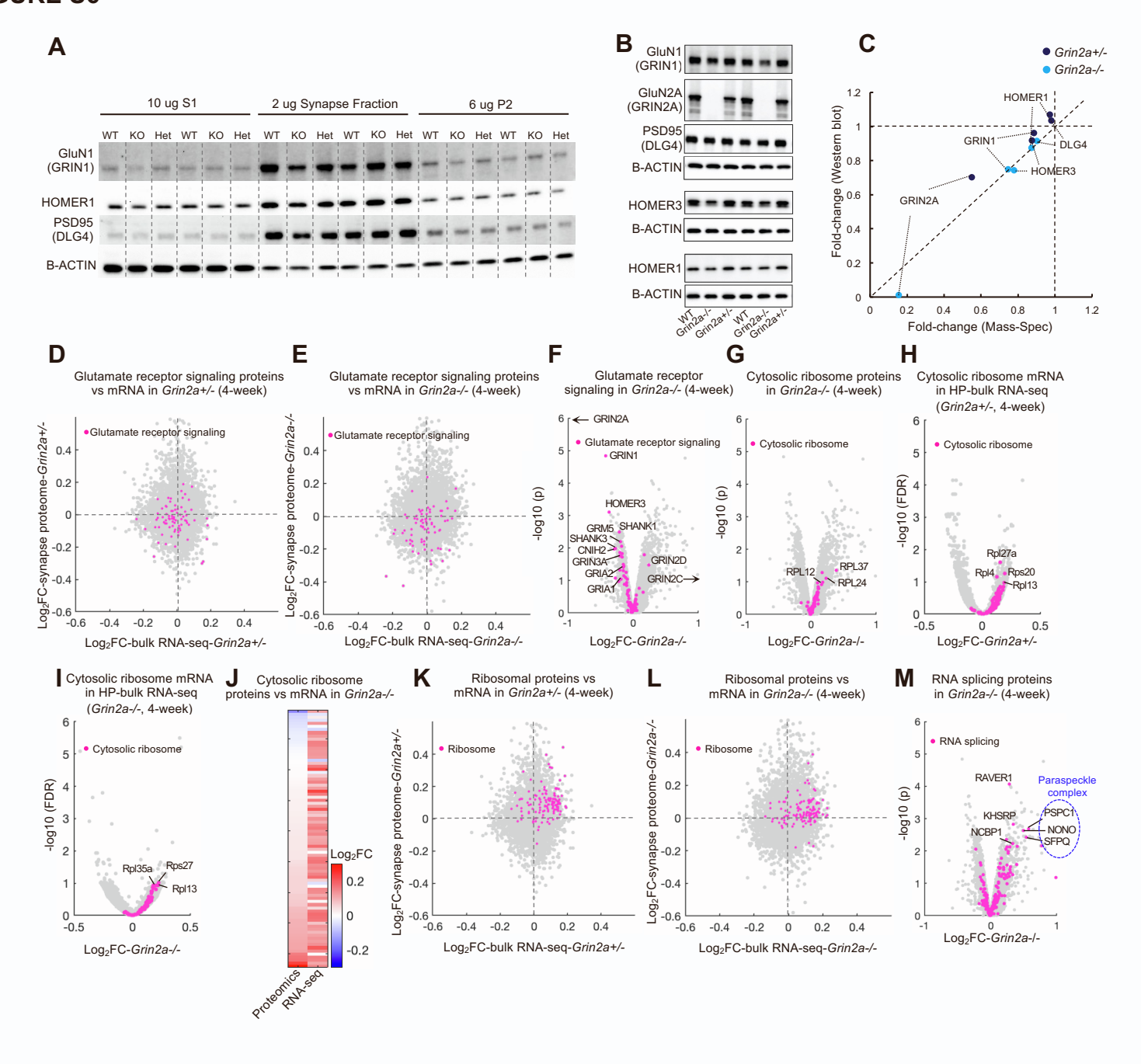


Figure S6. Alteration of glutamate receptor signaling and ribosomal proteins in synapse proteome of *Grin2a*^{-/-} mice, Related to Figure 6.

- (A) Western blots probing for GluN1, HOMER1 and PSD95 in S1, P2 and synapse fractions (see Methods) from wild type (WT), *Grin2a*^{+/-} (Het) and *Grin2a*^{-/-} (KO), showing enrichment of synaptic proteins in the synapse fraction.
- (**B**) Western blots probing for GluN1, GluN2A, PSD95, HOMER3 and HOMER1 in synaptic fractions from an independent cohort of *Grin2a* mutant mice.
- (C) Quantification of (B) against fold-changes obtained from proteomics data.
- (**D-E**) Transcriptomic changes in the hippocampal bulk RNA-seq data versus the hippocampal synaptic proteome changes in *Grin2a*^{+/-} (**D**) and *Grin2a*^{-/-} (**E**) at 4 weeks highlighting genes in the 'glutamate receptor signaling pathway' gene-set.
- (**F**) Volcano plot of proteomic changes in *Grin2a*^{-/-} synapses highlighting proteins in the 'glutamate receptor signaling pathway' gene-set.
- **(G)** Volcano plot of proteomic changes in *Grin2a*^{-/-} synapses highlighting proteins in the 'cytosolic ribosome' gene-set.
- (**H-I**) Volcano plots of the transcriptomic changes identified by bulk RNA-seq analysis in the hippocampus of $Grin2a^{+/-}$ (**H**) and $Grin2a^{-/-}$ (**I**) at 4 weeks highlighting genes in the 'cytosolic ribosome' gene-set.
- (**J**) Heatmap depicting all detected proteins in the 'cytosolic ribosome' gene-set in the hippocampal synaptic proteome and their mRNA changes in hippocampal bulk RNA-seq data in 4-week *Grin2a*^{-/-}.
- (**K-L**) Transcriptomic changes in the hippocampal bulk RNA-seq data versus the hippocampal synaptic proteome changes in *Grin2a*^{+/-} (**K**) and *Grin2a*^{-/-} (**L**) at 4 weeks highlighting genes in the 'Ribosome' GO term.
- (**M**) Volcano plot of proteomic changes in *Grin2a*^{-/-} synapses highlighting proteins in the 'RNA splicing' gene-set.

In **F** arrows indicate the proteins that are out of the range of the plots.

FIGURE S7

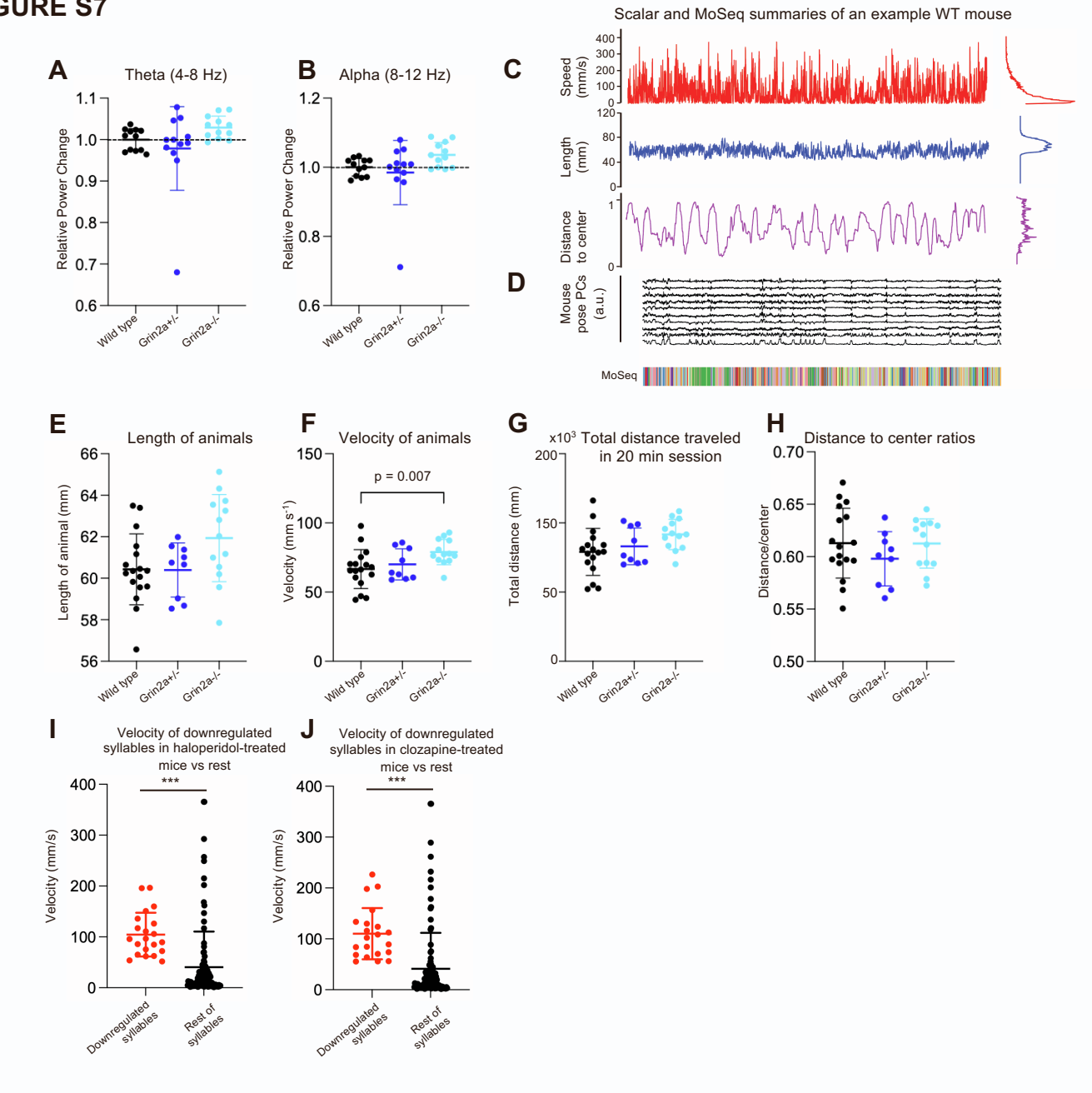


Figure S7. EEG and MoSeq characterization of *Grin2a* mutant mice, Related to Figure 7.

- (**A-B**) Power spectral density (PSD) changes in *Grin2a* mutant mice relative to wild-type animals at ~3 months of age, measured during NREM sleep during the light cycle for each of the frequency bands: (**A**) theta, 4-8 Hz; (**B**) alpha, 8-12 Hz gamma. Error bars show mean +/- standard error; n = 12 mice/group.
- (**C**) Temporal distribution of speed (mm/s), mouse length (mm), and distance-to-center ratio (with 0 representing the center and 1 representing the absolute margin of arena) for a representative wild-type mouse.
- (**D**) The top 10 principal component (PC) traces of the processed 3D depth images for an example wild-type mouse. The MoSeq Autoregressive Hidden Markov Model (AR-HMM) (see Methods) takes in the top 10 PC values as inputs and segments the depth videos into modulated behavioral motifs, referred to as syllables. For each mouse, a MoSeq-based behavioral summary was generated using 20 min of data (bottom).
- (**E-H**) Length (**E**), velocity (**F**), total distance traveled within a 20 min session (**G**), and distance to center ratio (**H**) are plotted per genotype. Error bars show mean +/- standard error; n = 17 wild type (WT), n = 9 *Grin2a*^{-/-}, n = 13 *Grin2a*^{-/-}. P values are computed using Welch's t test.
- (**I-J**) Mean velocity for downregulated syllables in haloperidol- (**I**) and clozapine- (**J**) treated mice (red box in **Fig. 7I**) versus rest of identified syllables. Error bars show mean +/- standard error. Asterisks (*) indicate statistical significance assessed using non-parametric permutation tests (see Methods); (***) indicates p < 0.001.